

Molecular Dynamics Simulations of Atmospheric Oxidants at the Air–Water Interface: Solvation and Accommodation of OH and O₃

John Vieceli,^{†,*} Martina Roeselová,^{†,§} Nicholas Potter,[†] Liem X. Dang,^{||} Bruce C. Garrett,^{||} and Douglas J. Tobias^{*,†}

Environmental Molecular Science Institute and Department of Chemistry, University of California, Irvine, California 92697-2025, Center for Biomolecules and Complex Molecular Systems, Institute of Organic Chemistry and Biochemistry, Academy of Sciences of the Czech Republic, Flemingovo nám. 2, 16610 Prague 6, Czech Republic, and Environmental Molecular Sciences Laboratory, Pacific Northwest National Laboratory, Richland, Washington 99352

Received: March 15, 2005; In Final Form: June 15, 2005

A comparative study of OH, O₃, and H₂O equilibrium aqueous solvation and gas-phase accommodation on liquid water at 300 K is performed using a combination of ab initio calculations and molecular dynamics simulations. Polarizable force fields are developed for the interaction potential of OH and O₃ with water. The free energy profiles for transfer of OH and O₃ from the gas phase to the bulk liquid exhibit a pronounced minimum at the surface, but no barrier to solvation in the bulk liquid. The calculated surface excess of each oxidant is comparable to calculated and experimental values for short chain, aliphatic alcohols. Driving forces for the surface activity are discussed in terms of the radial distribution functions and dipole orientation distributions for each molecule in the bulk liquid and at the surface. Simulations of OH, O₃, and H₂O impinging on liquid water with a thermal impact velocity are used to calculate thermal accommodation (*S*) and mass accommodation (α) coefficients. The values of *S* for OH, O₃, and H₂O are 0.95, 0.90, and 0.99, respectively. The approaching molecules are accelerated toward the liquid surface when they are approximately 5 Å above it. The molecules that reach thermal equilibrium with the surface do so within 2 ps of striking the surface, while those that do not scatter into the gas phase with excess translational kinetic energy in the direction perpendicular to the surface. The time constants for absorption and desorption range from approximately 35 to 140 ps, and the values of α for OH, O₃, and H₂O are 0.83, 0.047, and 0.99, respectively. The results are consistent with previous formulations of gas-phase accommodation from simulations, in which the process occurs by rapid thermal and structural equilibration followed by diffusion on the free energy profile. The implications of these results with respect to atmospheric chemistry are discussed.

I. Introduction

A detailed understanding of gas-phase uptake at liquid surfaces is necessary to understand a variety of processes occurring in the natural environment. This is particularly evident in the atmosphere, where aerosols provide an important mechanism for the removal and conversion of atmospheric gases.¹ Atmospheric gases that adsorb to a liquid aerosol surface diffuse in the particle and participate in homogeneous or heterogeneous chemical reactions with other species in the particle. The reaction products may remain in the particle, where they modify the physicochemical properties of the aerosol, or be released back to the gas phase to participate in further chemistry.

While the composition of atmospheric aerosol particles varies widely, the uptake of atmospheric oxidants, such as the OH radical and O₃, by aqueous aerosols is an active area of research due to the fact that they can reach appreciable concentrations in the lower atmosphere^{2,3} and participate in significant chemical reactions. In recent years, several studies demonstrate that the presence of aqueous aerosols may lead to potentially important

oxidation reactions with enhanced kinetics relative to the gas phase. In particular, OH and O₃ may play a significant role in heterogeneous aqueous aerosol chemistry in the marine boundary layer through reactions with halide ions at the surface of aqueous sodium halide aerosols,^{4–6} which result in the release of molecular halogens to the gas phase. In these reactions, the oxidants react with a component of the aerosol, but another possibility is that an oxidant may coadsorb with another gas-phase species and participate in a chemical reaction with enhanced kinetics, which is the case for gas-phase O₃ and dimethyl sulfide.⁷

Although the chemical reactions occurring in aqueous aerosols are of primary importance to atmospheric chemistry, a general consensus does not exist within the scientific community with regard to the proper formulation for nonreactive gas uptake by pure water, except that thermal equilibration occurs rapidly with a high probability per collision with the surface. In other words, the thermal accommodation coefficient (*S*) which is defined as

$$S = \frac{\text{number of impinging molecules equilibrated to liquid temperature}}{\text{number of molecules impinging on liquid surface}} \quad (1)$$

is near unity. Elucidating the characteristic features of nonre-

* To whom correspondence should be addressed. E-mail: dtobias@uci.edu.

[†] University of California.

[‡] Present address: Zymeworks, Inc., 201-1401 W. Broadway Ave., Vancouver, British Columbia, Canada V6H 1H6.

[§] Academy of Sciences of the Czech Republic.

^{||} Pacific Northwest National Laboratory.

active uptake at aqueous surfaces is crucial in understanding the kinetics and mechanisms of reactive uptake. For the remainder of this paper, we focus on the issue of nonreactive uptake, which is also termed accommodation.

One formulation for accommodation is derived from droplet train apparatus experiments with a comprehensive set of gas-phase species.^{8,9} In this model, it is predicted that there is a large free energy barrier to entering the bulk liquid from the surface, which is attributed to the adsorbed molecule being able to nucleate a cluster of a critical size with the solvent molecules. The nucleation model can be reinterpreted in terms of capillary wave theory, where the coordination number replaces the cluster size variable.¹⁰ In the capillary wave model, absorption occurs via a progressive increase in the coordination number.

Several groups dispute the nucleation model based on results from molecular dynamics (MD) simulations. From a simulation of ethanol accommodation by liquid water, Wilson and Pohorille report that a barrier does not exist for transfer of the adsorbed molecule from the surface to the bulk liquid at low aqueous concentrations of ethanol.¹¹ Rather, their simulation results show that accommodation is governed by diffusion on the free energy profile for transfer of the gas-phase molecule into the bulk liquid. Subsequent computer simulations of a thermal gas-phase molecule impinging on an aqueous surface support the findings of Wilson and Pohorille. These studies include ethanol,¹² ethylene glycol,¹³ methanol,¹⁴ HO₂,¹⁵ H₂O,^{16,17} and OH¹⁸ on liquid water and OH and O₃ on aqueous sodium halide solutions.¹⁹ Free energy profiles calculated for N₂ and CO₂ from MD *do* exhibit a small barrier on the order of less than 1 kcal/mol at 300 K, but the generality of this result is not clear since Ar and CH₃CN do not.^{20,21} Recent work by Jungwirth and co-workers also supports the presence of a small barrier, which may be within the error of the calculation, for the transfer of adsorbed N₂, O₂, and O₃ into the bulk liquid, but a barrier is not present for the transfer of OH, HO₂, and H₂O₂.²² A general feature of the free energy profiles for N₂, CO₂, Ar, CH₃CN, O₂, O₃, OH, HO₂, and H₂O₂ is the existence of a surface minimum.

While the nucleation model uses the cluster size as the reaction coordinate, the free energy profiles from MD simulations use the distance between the incident molecule and the center of the water slab. This makes a direct comparison between the different formulations impossible. Furthermore, there is debate surrounding the mass accommodation coefficient, α , which measures the probability that a species striking the liquid surface is solvated in the liquid. This quantity appears in a phenomenological model of gas uptake, the resistor model, which couples the independent processes of mass accommodation, liquid-phase transport, and gas-phase transport using an electrical resistance model.⁹ Use of the resistor model to extract α values for various gas-phase species from droplet train experiments results in values dramatically different from those obtained using MD simulations. Again though, this comparison is complicated by differences in the length and time scales between the experiments and simulations and by the inherently ideal nature of the simulation systems. Morita and co-workers are actively investigating potential sources of this discrepancy using computational fluid dynamics and MD simulations.^{16,23–25}

The lack of agreement about critical features of the gas-phase accommodation process and fundamental quantities describing the process, such as α , indicates that further work is necessary for development of a detailed understanding of this process at aqueous surfaces. In this paper, *ab initio* calculations and MD simulations are used to study OH, O₃, and H₂O equilibrium

aqueous solvation and gas-phase accommodation on liquid water at 300 K. Previous work by Roeselová et al.^{18,19} and Viecele et al.¹⁷ on the accommodation of these species is extended in this study by using a more comprehensive set of computer simulation techniques and revised polarizable intermolecular potential parameters for OH and O₃ with water. A constrained MD technique is used to calculate the free energy profiles for the transfer of OH and O₃ from the gas phase to bulk water. Separate equilibrium simulations are used to study the aqueous solvation of OH and O₃ at the surface and in the bulk liquid, which is compared to that for neat water. OH, O₃, and H₂O scattering trajectories provide molecular-scale detail about the accommodation process. By preparing 250 initial conditions with a single gas-phase molecule approaching the surface of liquid water with a thermal impact velocity, one determines S and α and the characteristic kinetics and mechanisms of the accommodation process. Finally, a preliminary assessment of different reaction coordinates for the accommodation process is presented.

The remainder of this paper is organized as follows. The systems and methodologies of the various simulations are described in section II. The results and discussion are presented in section III, and the conclusions are given in section IV. The implications of this work with respect to heterogeneous chemistry in the atmosphere are briefly discussed in section V.

II. Systems and Methods

A comprehensive set of simulations is used to study the solvation and accommodation of OH, O₃, and H₂O in liquid water. The details of *ab initio* calculations, cluster simulations, and MD simulations of extended aqueous slab systems, including constrained, scattering, and equilibrium dynamics, are provided in this section. MD simulations of the extended systems are performed using a slab of water molecules with two independent vacuum–water interfaces on each side at 300 K. The vacuum–water interface used in these simulations is a reasonable model for a small patch of an air–water interface²⁶ considering that less than one nitrogen molecule, which is the most abundant gas in air, should be included in the vacuum region based on the density of nitrogen in air and the free volume of the simulation box. The region between 90 and 10% of the bulk water density operationally defines the interface, and since the z dimension is perpendicular to the interface, the z values at these densities are denoted by z_{90} and z_{10} , respectively. The middle of the interface region corresponds to the Gibbs dividing surface, where the density is 50% of the bulk liquid, and is denoted by z_{GDS} .

The simulations utilize intermolecular potentials that explicitly include the induced polarization. Recent computational studies of the surfaces of aqueous clusters and solutions containing polarizable anions, such as Cl[−], Br[−], I[−], NO₃[−], and SO₄^{2−}, indicate that polarizability is crucial for accurate structural predictions.^{26–29} Although the systems studied here do not contain ions, polarizable force fields for OH and O₃ are developed for use in future simulations with ions. The water molecules are described using the polarizable model developed by Caldwell and Kollman, POL3.³⁰ POL3 provides an accurate description of the bulk³⁰ and surface¹⁷ properties of liquid water.

A. *Ab Initio* Calculations and Cluster Simulations. The *ab initio* optimizations and calculations of molecular polarizabilities of OH and O₃ are performed at the MP2/aug-cc-pvtz level using the Gaussian 98 program package.³¹ For geometry optimizations of the small OH–water and O₃–water clusters with the empirical force field, version 5 of the AMBER program package is used.³² AMBER 5 is also used to carry out the

simulations of the larger $\text{OH}(\text{H}_2\text{O})_n$ clusters ($n = 4-7$) at 150 and 300 K in the canonical (NVT) ensemble. The systems are simulated for 200 ps.

B. Constrained Molecular Dynamics Simulations. The free energy profiles for the transfer of OH and O_3 from the gas phase to the bulk liquid at 300 K are calculated as a potential of mean force using a constrained molecular dynamics technique in the canonical ensemble.³³ The liquid slab contains 600 water molecules and a single solute in a simulation box with dimensions of 26.3 Å (x) \times 26.3 Å (y) \times 76.3 Å (z). Three-dimensional periodic boundary conditions are applied. These simulations were performed at Pacific Northwest National Laboratory using a modified version of AMBER 4.³⁴

The free energy difference, $\Delta F(z_s)$, between a state when the solute is located at z_s and a reference state when the solute is at z_0 is calculated according to

$$\Delta F(z_s) = F(z_s) - F_0 = \int_{z_0}^{z_s} \langle f_z(\zeta) \rangle d\zeta \quad (2)$$

where $f_z(\zeta)$ is the z component of the total force exerted on the solute at a given z position, z_s , averaged over the canonical ensemble. The free energy profile is defined up to an arbitrary additive constant, F_0 , corresponding to the free energy of a reference state, which is chosen to be the slab with the solute located in the gas phase. At each z position of the solute, incremented by 1 Å, the averaging of $f_z(\zeta)$ is carried out over 350 ps after an initial 100 ps equilibration period. By averaging separately over the first and last 175 ps of the simulation at each z position of the solute, we estimate the error of the calculated free energy values (± 0.1 kcal/mol) by taking the difference between the corresponding two values of free energy.

Strictly speaking, eq 2 is defined in a canonical ensemble, and yields a Helmholtz free energy difference, ΔF . In our simulation, the total volume of the system is fixed. However, because the open interfaces allow the volume of the water slab to fluctuate, the conditions of the simulation actually resemble the isothermal–isobaric (NPT) ensemble. Thus, the calculated free energies are directly compared to the experimentally accessible Gibbs free energies, ΔG .¹³

C. Scattering and Equilibrium Simulations. The scattering and equilibrium simulations are performed in the microcanonical (NVE) ensemble using a simulation box with dimensions of 30 Å (x) \times 30 Å (y) \times 100 Å (z) and three-dimensional periodic boundary conditions. Initial conditions for the accommodation study are obtained from a 250 ps equilibrium simulation of 864 water molecules at 300 K. By taking configurations every 50 ps, we generate five initial configurations. For each configuration, a single gas-phase molecule, OH, O_3 , or H_2O , is placed at $z = 30$ Å, approximately 15 Å above one of the air–water interfaces. The velocity of each atom is assigned from a Maxwell–Boltzmann (MB) distribution at 300 K, subject to the constraint that the molecular center of mass velocity in the z dimension is directed toward the nearest interface. Placing the molecule at 50 different grid points in the x – y plane for each of the five initial configurations of the water slab generates a total of 250 trajectories for each molecule. Each trajectory is propagated for 90 ps.

The equilibrium solvation of OH and O_3 in water is studied by restarting configurations from the end of the 90 ps trajectories with random velocities sampled from the MB distribution at 300 K. Initial configurations with the solute in bulk water and at the interface are used to generate 60 trajectories that are 50 ps long, giving a total of 3.0 ns of equilibrium sampling for each solute. These simulations are used to calculate the radial

TABLE 1: OH Force Field Parameters^a

| force field | q (e) ^b | α (Å ³) ^c | $r_m/2$ (Å) ^d | ϵ (kcal/mol) |
|-------------------|----------------------|---|--------------------------|-----------------------|
| OH1 ^e | | | | |
| O | −0.4 | 1.07 | 1.798 | 0.156 |
| H | 0.4 | 0.0 | 0.0 | 0.0 |
| OH2 ¹⁹ | | | | |
| O | −0.4 | 0.528 | 1.798 | 0.156 |
| H | 0.4 | 0.170 | 1.320 | 0.022 |

^a $r_{\text{eq}} = 0.967$ Å. ^b Atomic charge. ^c Atomic polarizability. ^d Half the interatomic separation at the minimum of the Lennard-Jones potential. ^e Present force field.

distribution functions and dipole orientation distributions for OH and O_3 molecules in bulk water and at the air–water interface. For comparison, these distribution functions are calculated for H_2O from the 250 ps simulation that generates the initial conditions for the accommodation study. Version 6 of the AMBER software package³⁵ is used to perform the scattering and equilibrium simulations on the Medium Performance Computing Beowulf Cluster at the University of California (Irvine, CA).

D. Molecular Dynamics Simulation Methodology. In this section, the standard methodology used for all of the classical molecular dynamics simulations is described. The electrostatic interactions are calculated using the smooth particle mesh Ewald method.³⁶ The induced dipoles are determined self-consistently using the standard iterative procedure.^{37,38} This procedure is summarized as follows. (a) At every dynamical time step, the electric field at atom i produced by the fixed charges in the system is computed. (b) The calculated electric field is then used to generate the initial estimate of the induced dipole moments. (c) The initial estimate of the induced dipoles and the calculated electric field are used to compute the total electric field. Steps b and c are repeated until the deviations of the induced dipoles between two sequential iterations fall below a set tolerance value.

All bond lengths and angles are constrained to their equilibrium values using the SHAKE algorithm,³⁹ which is expected to have a negligible effect on the results of the scattering simulations with a thermal impact velocity. This is because vibrational excitations are unlikely to be caused by thermal collisions. A time step of 1.0 fs is used. The temperature of simulations in the canonical ensemble is regulated using the Berendsen scheme.⁴⁰

III. Results and Discussion

A. Potential Parameters and Force Field Validation. A polarizable force field for OH and O_3 is developed on the basis of known experimental and ab initio data for the isolated gas-phase species and their complexes with water. In general, polarizability is an overall, nonadditive property of the whole system. However, for noncovalently interacting particles, it can be to a very good approximation constructed from contributions of individual atoms and molecules comprising the systems.⁴¹ Therefore, to describe OH and O_3 interacting with water, it is sufficient to supplement the existing POL3 model parameters with suitable parameter sets for the two solutes. Among several different parameter sets that are tested in the process, we choose the set for each species that most closely reproduces the experimental hydration free energy.

1. Hydroxyl Radical. The OH parametrization employed in this work, as well as in our recent communication,¹⁸ denoted by OH1 in Table 1, represents a refinement of the force field used by some of us in the original study of OH interacting with

TABLE 2: Comparison of OH Force Fields

| | ΔE (kcal/mol) ^a | $r(\text{O}–\text{O})$ (Å) ^b | ΔG_s (kcal/mol) ^c |
|----------------------------|------------------------------------|---|--------------------------------------|
| OH1 | −7.4 | 2.7 | −3.0 |
| OH2 ¹⁹ | −3.9 | 3.4 | −1.0 |
| ab initio ^{44–48} | −5.5 to −6.7 | ~2.9 | — |
| experimental | — | 2.9 ⁵¹ | −3.9 ^{49,50} |

^a Binding energy of the OH···H₂O complex. ^b Oxygen–oxygen distance in the OH···H₂O complex. ^c Free energy of aqueous solvation.

the air–water interface.¹⁹ In the original force field (OH2), the atomic polarizabilities of oxygen and hydrogen from the POL3 model are used. For the new force field, an ab initio calculation of OH polarizability is performed and the atomic polarizabilities are reassigned. In addition, the Lennard-Jones parameters of the OH hydrogen atom are set to zero, analogous to the POL3 model. The force field parameters are summarized in Table 1.

a. Polarizability. The polarizability of an isolated OH is calculated using the MP2 approach. The final results, converged within less than 10% with respect to the basis set, are obtained at the MP2/aug-cc-pvtz level. The results are in very good agreement with previous ab initio calculations.⁴² To the best of our knowledge, no experimental data are available for comparison. The polarizability tensor exhibits only a modest anisotropy ($\alpha_{xx} - \alpha_p = 0.01 \text{ \AA}^3$, $\alpha_{yy} - \alpha_p = -0.19 \text{ \AA}^3$, $\alpha_{zz} - \alpha_p = 0.18 \text{ \AA}^3$). Thus, to a good approximation, the molecular polarizability of OH can be represented by the isotropic polarizability ($\alpha_p = 1.07 \text{ \AA}^3$), which is defined by the average of the diagonal terms of the polarizability tensor. In the force field, the entire value of the isotropic polarizability is assigned to the oxygen atom.

To assess the effect of the aqueous environment on the OH polarizability, we included in the ab initio calculation the surrounding water molecules, which are represented by the fractional point charges at the atomic positions.⁴³ For this purpose, 20 snapshots from a classical MD simulation of OH interacting with an extended aqueous slab are used, where OH is in the bulk for 10 snapshots and at the interface for the other 10. These calculations yield an α_p in the range of 1.04–1.06 \AA^3 . No systematic differences between the configurations with OH in the bulk and at the interface are observed. In summary, the solvent effect on the polarizability of OH, unlike in the case of solvated ionic species,^{28,29,43} is negligible. Therefore, the gas-phase α_p value of 1.07 \AA^3 is adopted in the OH1 force field.

b. Force Field Development. As a first step, the OH force field is tested against ab initio calculations for the OH···H₂O complex.^{44–48} In addition, the free energy profile for transfer of OH across the air–water interface is calculated to compare the resulting free energy of hydration, ΔG_s , with the experimental value, $\Delta G_{s,\text{exp}}$.^{49,50} Table 2 summarizes the results and presents a comparison of the current force field, OH1, with the original force field, OH2.¹⁹

In terms of OH–H₂O binding, both sets give a planar (C_{2v}) geometry of the complex, in which OH acts as a proton donor and water as a proton acceptor (Figure 1). Although the ab initio optimizations yield a geometry with the water hydrogen atoms tilted by $\sim 35^\circ$ from the plane defined by the atoms of OH and the water oxygen atom, the planar geometry of the complex corresponds to a structure averaged over the zero-point vibrational motion (flipping) of the water H atoms above and below the plane. Thus, the planar geometry of the OH···H₂O complex obtained using the empirical force field is in excellent agreement with experimental⁵¹ and ab initio results,^{48,51} which predict a marginal energy difference between the minimum and the planar structure. However, the OH2 parametrization underestimates

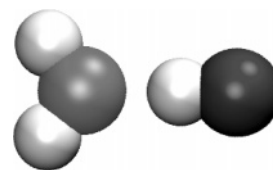


Figure 1. Optimized geometry of the OH···H₂O complex (the oxygen atom of the OH radical depicted in dark gray).

both the stabilization energy of the complex, ΔE , and the free energy of solvation, ΔG_s . The weak OH–H₂O interaction can be rationalized in terms of the low OH polarizability and the non-zero Lennard-Jones parameters on the OH hydrogen atom and is reflected in a large $r(\text{O}–\text{O})$ distance.

In an attempt to remedy this unphysical behavior, the OH1 parameter set is developed, in which the atomic polarizabilities for oxygen and hydrogen are reassigned and the Lennard-Jones parameters for hydrogen are set to zero (as is the case for POL3 hydrogen atoms). These changes result in a substantial improvement in the performance of the force field in all aspects.

c. Microsolvation Modeling. The OH1 force field is further tested for its ability to correctly model the microsolvation of OH in small OH(H₂O)_{*n*} clusters (*n* = 1–7). These clusters are the subject of two recent theoretical investigations.^{44,45} Both of the studies predict cluster structures in which OH participates in two hydrogen bonds (acting as a proton donor and proton acceptor) to be the energetically most favorable. This is also the case when modeling the small OH(H₂O)_{*n*} clusters with the empirical force field.

For the three smallest clusters (*n* = 1–3), geometry optimization is performed, resulting, when *n* = 1, in the OH···H₂O complex structure mentioned above. When *n* = 2–3, the optimization yields cyclic structures similar to those of the water trimer and the water tetramer, in agreement with the ab initio results. For larger clusters (*n* = 4–7), MD simulations at 150 and 300 K are performed, initiated from several different configurations, including those in which OH is located inside a cage or a ring of water molecules as well as those in which OH is attached to a water cluster from outside, hydrogen-bonded to one of the water molecules in the proton donor fashion. In the former case, OH leaves the interior of the cage very fast, within the first few picoseconds, and is incorporated into the hydrogen bonding network of the water molecules. In the latter case, the cluster rearranges and OH quickly forms hydrogen bonds at both ends. No substantial difference between the configurations sampled at 150 and 300 K is observed. The kinetic energy at the higher temperature is deposited predominantly into the overall rotation of the cluster.

The OH(H₂O)₄ and OH(H₂O)₅ clusters adopt a cyclic geometry typically within less than 50 ps, around which they oscillate until the end of the 200 ps simulation. Similar behavior is also observed for the OH(H₂O)₆ cluster; however, other configurations (such as the “book”-like structure consisting of one four-membered and one five-membered ring fused together) are also sampled occasionally for a short time. The largest cluster that has been studied, OH(H₂O)₇, no longer prefers the cyclic structure. Being already rather flexible, it samples various configurations, mostly consisting of several four- and five-membered rings. As an illustration, Figure 2 shows several snapshots from a simulation of the OH(H₂O)₇ cluster at 150 K, started from a structure in which OH is embedded in a “cage” of water molecules (Figure 2a). To construct the initial configuration, a snapshot is taken from a trajectory of OH solvated in liquid water and the seven nearest water molecules are selected. In this cluster, OH almost immediately moves to the outside of

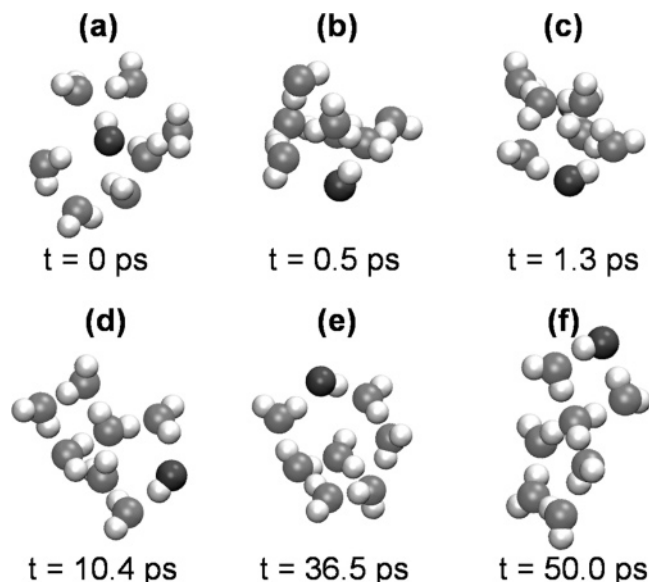


Figure 2. Snapshots from a simulation of the $\text{OH}(\text{H}_2\text{O})_7$ cluster at 150 K with a polarizable force field (the oxygen atom of the OH radical depicted in dark gray).

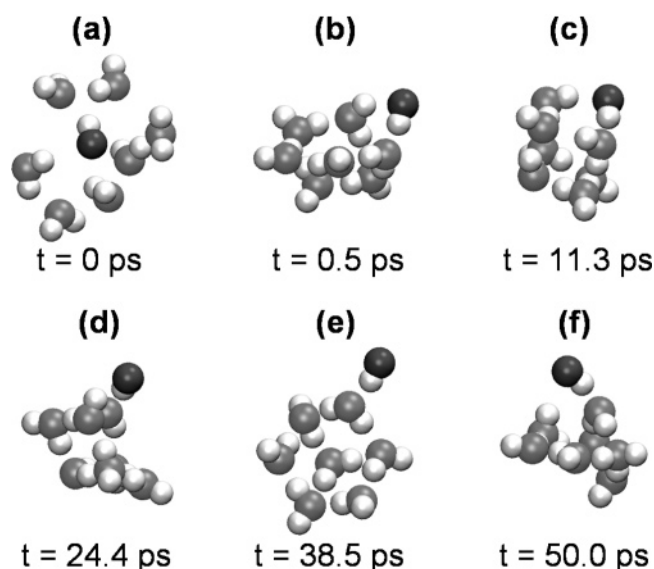


Figure 3. Snapshots from a simulation of the $\text{OH}(\text{H}_2\text{O})_7$ cluster at 150 K with a nonpolarizable force field (the oxygen atom of the OH radical depicted in dark gray).

the water cage and forms a hydrogen bond (as a proton donor) to an oxygen atom of one of the water molecules (Figure 2b). Within ~ 1 ps, another hydrogen bond is formed, in which OH participates as a proton acceptor (Figure 2c). Later, OH remains located on the cluster “surface”, participating predominantly in a four-membered ring similar to the $\text{OH}(\text{H}_2\text{O})_3$ structure (Figure 2d,f). Because of the remarkable stability of the four-membered ring structure,⁴⁴ this motif is one of the basic “building units” of the $\text{OH}(\text{H}_2\text{O})_n$ clusters.

In summary, the structural properties of $\text{OH}(\text{H}_2\text{O})_n$ clusters predicted with the current force field are in good agreement with the *ab initio* results. In these clusters, OH typically participates in two hydrogen bonds, being both a proton donor and a proton acceptor. In comparison to the *ab initio* results, the empirical force field seems to overestimate the stability of the cyclic structures when $n = 4-6$. It is interesting to note that polarizability seems to play an important role in correctly reproducing the structures of the $\text{OH}(\text{H}_2\text{O})_n$ clusters with the

TABLE 3: O_3 Force Field Parameters^a

| force field | q (e) ^b | α (\AA^3) ^c | $r_m/2$ (\AA) ^d | ϵ (kcal/mol) |
|---------------------|----------------------|--|---------------------------------------|-----------------------|
| OZ1 ^e | | | | |
| O _{center} | 0.19 | 0.95 | 1.661 | 0.210 |
| O _{side} | −0.095 | 0.95 | 1.661 | 0.210 |
| OZ2 ⁶ | | | | |
| O _{center} | 0.19 | 0.95 | 1.798 | 0.156 |
| O _{side} | −0.095 | 0.95 | 1.798 | 0.156 |
| OZ3 ¹⁹ | | | | |
| O _{center} | 0.12 | 0.77 | 1.798 | 0.156 |
| O _{side} | −0.06 | 0.77 | 1.798 | 0.156 |

^a $r_{\text{eq}} = 1.28$ \AA ; $\theta_{\text{eq}} = 116.7^\circ$.¹⁹ ^b Atomic charge. ^c Atomic polarizability. ^d Half the interatomic separation at the minimum of the Lennard-Jones potential. ^e Present force field.

empirical force field. In simulations with a nonpolarizable potential,²² which are carried out for comparison, OH is found to be a much weaker hydrogen bond acceptor. The ring structure of the smaller clusters repeatedly breaks and re-forms during the simulation. The larger clusters exhibit a substantially greater flexibility than when polarizability is included, undergoing much rearrangement and sampling, to a great extent, the configurations in which OH is attached to the water cluster as a proton donor, forming only one hydrogen bond to the nearest water molecule. This is illustrated in Figure 3, which shows several snapshots from a simulation of the $\text{OH}(\text{H}_2\text{O})_7$ cluster at 150 K with a nonpolarizable force field, started from the same initial cage structure (Figure 3a) as in the simulation with the polarizable potential (compare to Figure 2a).

Because of its radical character, it is rather difficult to accurately describe OH by a simple empirical force field, yet the good agreement between ΔG_s and the experimental value^{49,50} coupled with the satisfactory performance of the present force field in terms of OH microsolvation in clusters^{44,45} indicates that MD simulations with empirical potentials can provide very useful insight into processes at the air–water interface involving the OH radical.

2. *Ozone*. For the purposes of this work, a polarizable O_3 force field is developed using a new parameter set. Again, the prime concern is the ability of the force field to reproduce $\Delta G_{s,\text{exp}}$. The potential parameters of the present force field, OZ1, are summarized in Table 3. For comparison, this table also contains two previous parameter sets, OZ2⁶ and OZ3.¹⁹

a. *Polarizability*. Previous experimental^{52,53} and theoretical⁵⁴⁻⁵⁶ studies of the electric properties of O_3 , including the dipole and quadrupole moments and dipole polarizability, are available in the literature. For the present force field, OZ1, as well as for OZ2, the isotropic polarizability ($\alpha_p = 2.85$ \AA^3) calculated at the CCSD(T)/7s5p4d2f level is adopted.⁵⁵ Both the isotropic polarizability and polarizability anisotropy ($\alpha_{xx} - \alpha_p = 6.3501$ \AA^3 , $\alpha_{yy} - \alpha_p = -3.8418$ \AA^3 , and $\alpha_{zz} - \alpha_p = -2.5083$ \AA^3) are in very good agreement with the results obtained at the CASPT2 level,⁵⁶ as well as with experimental data.^{52,53} As for OH, the solvent effect on O_3 polarizability is expected to be negligible. Therefore, the gas-phase α_p is used in the force field. One-third of this value ($\alpha_p/3 = 0.95$ \AA^3) is assigned to each of the oxygen atoms.

b. *Force Field Development*. The equilibrium bond length and angle are adopted from the original force field, OZ3.¹⁹ The atomic charges are chosen to match the experimental value of the permanent dipole moment (0.53 D) in the equilibrium geometry.^{52,53} In terms of the Lennard-Jones parameters, two sets are successively tested: the oxygen parameters from the

TABLE 4: Comparison of O₃ Force Fields

| | ΔE (kcal/mol) ^a | $r(\text{O}_{\text{center}}-\text{O}_{\text{w}})$ (Å) ^b | ΔG_{s} (kcal/mol) ^c |
|----------------------------|------------------------------------|--|---|
| OZ1 | −1.46 | 3.07 | 0.62 |
| OZ2 | −1.30 | 3.19 | 1.60 |
| OZ3 | −0.94 | 3.26 | — |
| ab initio ^{58,59} | −0.7 to −2.4 | ~2.9 | — |
| experimental | — | 2.96 ⁵⁹ | 0.84 ± 0.07 ⁴⁹ |

^a Binding energy of the O₃···H₂O complex. ^b O₃ center oxygen–water oxygen distance in the O₃···H₂O complex. ^c Free energy of aqueous solvation.

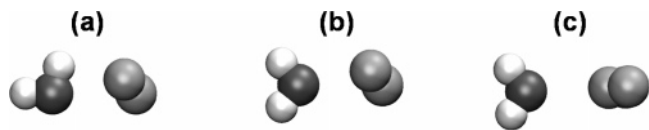


Figure 4. Most stable structure of the O₃···H₂O complex: (a and b) inferred from experiment and/or suggested by ab initio calculations^{58,59} and (c) obtained from the optimization with the present force field, OZ1.

POL3³⁰ model in OZ2 and OZ3 and Jorgensen's OPLS⁵⁷ parameters for a carbonyl carbon in OZ1, which is used in this study.

To assess the performance of the empirical force field, its predictions for the O₃···H₂O complex are compared against ab initio calculations.^{58,59} For larger O₃–H₂O clusters, involving more than one water molecule, no data are available in the literature. The results are summarized in Table 4.

Due to the increased magnitude of the permanent dipole moment and α_{p} in OZ2 relative to OZ3, ΔE is stabilized by 40%. Changing the Lennard-Jones parameters from those of OZ2 to those of OZ1 results in a further stabilization of ΔE by approximately 10%. All three values of ΔE fall within the range of calculated ab initio values reported in the literature.^{58,59}

The ab initio investigation of the O₃···H₂O complex represents a rather demanding task. It is well-known that reliable predictions for van der Waals complexes involving O₃ require large basis sets, accurate treatment of the electron correlation, and, ideally, description going beyond one Slater determinant. A few ab initio calculations at various levels of theory for the O₃···H₂O complex result in several minima localized at the O₃–H₂O potential energy surface; however, the optimal structure is not unequivocally resolved. The O₃–H₂O interaction is not yet fully understood, and the geometry of the O₃···H₂O complex remains a controversial issue. The two most promising candidates for the O₃···H₂O structure (Figure 4a,b), whose rotational constants agree with the experimental data,⁵⁹ are both stabilized by the dipole–dipole interaction. In addition, a substantial transfer of the electron density from O₃ to H₂O seems to be involved in the binding. The structures in which the water molecule is hydrogen bonded to one of the terminal oxygen atoms of O₃ are found to be less stable.

Obviously, the empirical force field is limited in describing the complex bonding nature between O₃ and H₂O. In agreement with the experimental and theoretical predictions, geometry optimization with the present force field yields a structure of the O₃···H₂O complex that is stabilized by the dipole–dipole interaction. Also, $r(\text{O}_{\text{center}}-\text{O}_{\text{w}})$ is reproduced reasonably well. However, the empirical force field results in a preference for the arrangement of the O₃···H₂O complex in which the dipole moments of the two monomers are aligned parallel to one another (Figure 4c), unlike the structures inferred from experiments and suggested by the ab initio studies (Figure 4a,b). In any case, the present force field seems to capture the most substantial aspects of the binding. The subtle issue of the mutual

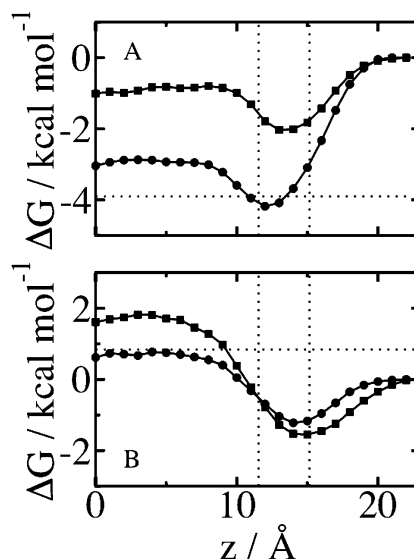


Figure 5. Free energy profiles for the transfer of (A) OH and (B) O₃ across the air–water interface calculated with different force field parametrizations. The vertical dotted lines denote the interface region, where the gas phase is to the right of the interface and the bulk liquid to the left. The horizontal dotted line in each panel corresponds to the experimental solvation free energy: (A) OH1 (●) and OH2 (■) and (B) OZ1 (●) and OZ2 (■).

orientation of the two monomers in the gas-phase O₃···H₂O complex is not likely to play a crucial role in simulations involving many water molecules, such as when studying O₃ in contact with liquid water.

In terms of O₃ solvation in liquid water, the performance of the empirical force field is tested by calculation of the free energy profile for transfer of O₃ across the air–water interface. In Table 4, the resulting ΔG_{s} is compared to $\Delta G_{\text{s,exp}}$, which corresponds to the Henry's law constant, k_{H} , in the range between 0.009 and 0.012 M/atm.⁴⁹ The increase in free energy upon hydration reflects the poor aqueous solubility of O₃. OZ2 overestimates $\Delta G_{\text{s,exp}}$ by a factor of 2. Consequently, the aqueous solvation of O₃ modeled by OZ2 is even less favorable in the simulation than under experimental conditions. This undesirable aspect of OZ2 is improved in OZ1. The change in the oxygen Lennard-Jones parameters from those of OZ2 to those of OZ1 results in a decrease in ΔG_{s} , which is in very good agreement with $\Delta G_{\text{s,exp}}$.

In summary, the new polarizable potential for O₃ satisfactorily reproduces the hydration properties, as well as important aspects of O₃–H₂O binding. Nevertheless, in light of the importance of the O₃–H₂O interaction in the atmosphere, the investigation, both experimental and theoretical, of larger O₃–H₂O clusters, as well as development of a more sophisticated O₃ force field (including perhaps a quadrupole moment of O₃), is highly desirable.

B. Equilibrium Solvation of OH and O₃. 1. Free Energy Profiles. To assess the equilibrium solvation of OH and O₃, the free energy profiles for transfer across the air–water interface are evaluated. In Figure 5, the results are shown for OH1 and OH2 in the top panel and for OZ1 and OZ2 in the bottom panel. While the aqueous solvation of OH is attended by a decrease in the free energy, the free energy of O₃ is lower in the gas phase than in the bulk liquid, reflecting its poor aqueous solubility. As mentioned above, ΔG_{s} calculated with the final force field parametrizations (OH1 and OZ1) are in very good agreement with $\Delta G_{\text{s,exp}}$. The agreement between ΔG_{s} and $\Delta G_{\text{s,exp}}$ is one of the main benchmarks in the process of our

force field development since this quantity is considered to be crucial for accurate modeling of the gas-phase uptake process.

As can be seen from the comparison of the free energy curves obtained for different parameter sets, achieving reasonable agreement with experiment represents a nontrivial task, as the asymptotic value of the free energy in the liquid depends strongly on the choice of the force field. However, for both OH and O₃, different parameter sets consistently yield a minimum of the free energy in the interfacial region, which is ~1 kcal/mol lower than the free energy of OH in the bulk liquid or that of O₃ in the gas phase. The relative position of the free energy minimum within the interfacial layer reflects the differences between the individual parameter sets in terms of the solute–water interaction. With an increasing strength of ΔE , the free energy minimum is located deeper in the interface, at a z position corresponding to a greater water density. This is even more apparent when comparing the behavior of the two solutes. OH prefers to be located deep inside the interfacial layer, near z_{90} , whereas O₃ favors a location in the outermost region of the air–water interface, near z_{10} .

The existence and depth of the surface minimum appear to be rather robust, as similar results are reported in MD studies of other gas-phase molecules at the air–water interface, in which different (nonpolarizable) force fields for both water and the solutes are employed.^{20,22} In this connection, it is interesting to note that polarizability apparently does not play a critical role in the propensity of OH and O₃ for the air–water interface, although it is likely to be important for modeling the micro-solvation environment around these two solutes. The calculations indicate that, despite very different aqueous solvation behavior of OH and O₃, both species share a rather strong preference for being partially solvated at the air–water interface.

Another feature of the free energy profiles is relevant to the accommodation of gas-phase species in liquids. These profiles show no evidence for the existence of a barrier for transfer from the surface to the bulk liquid, regardless of the parameter set considered. One may expect a barrier for this transfer based on the nucleation model discussed in the Introduction; however, the reaction coordinate for an incoming molecule at the liquid surface in the nucleation model is the cluster size rather than the distance from the center of the bulk liquid. After the equilibrium and scattering simulations are discussed, the existence of a free energy barrier as a function of cluster size is investigated in section III.C.5.

2. Thermodynamic Surface Excess. These free energy profiles indicate that there is an enhancement in the concentration of OH and O₃ at the surface due to the free energy minimum. In addition to other atmospherically relevant gases discussed above, the magnitude of the surface minimum is comparable to those of ethylene glycol, methanol, and ethanol,^{11–13} which suggests that OH and O₃ may be considered surfactants on water. To quantitatively investigate this prediction, the surface excess, Γ , is calculated and compared to experimental and calculated values for the surface excess of methanol and ethanol.

Given the free energy profile for a solute i , Γ_i is given by¹¹

$$\Gamma_i = \int_{z_1}^{z_{\text{GDS}}} [c(z) - c_g] dz + \int_{z_{\text{GDS}}}^{z_g} [c(z) - c_l] dz \quad (3)$$

$$c(z) = c_g e^{-\beta \Delta G(z)} = c_l e^{-\beta \Delta G_s} e^{-\beta \Delta G(z)} \quad (4)$$

In eq 3, $c(z)$ is the concentration profile in the z dimension, c_g and c_l are the solute concentrations in the gas and liquid phases, respectively, z_g and z_l are positions that are sufficiently far from the interface in the gas and liquid phases, respectively, and z_{GDS}

is the position of the Gibbs dividing surface. (z_{GDS} is a standard reference value that is used since it yields a $\Gamma_{\text{H}_2\text{O}}$ of 0 by definition.) The values of $c(z)$ are determined using eq 4, where ΔG_s is the solvation free energy for transfer from the gas phase to the bulk liquid and $\Delta G(z)$ is the free energy value from the computed profile. For a given surface area, A , ΓA is the excess number of molecules in the surface region relative to the number expected if the bulk and gas-phase densities remain constant up to the dividing surface.⁶⁰

For a given value of c_g or c_l , the value of Γ for different solutes can be compared. The value of 0.0012 mol cm⁻³ is selected for c_l since it is sufficiently low that solute–solute interactions can be neglected and Γ_{OH} and Γ_{O_3} can be directly compared to previously calculated values for methanol (1×10^{-10} mol cm⁻²) and ethanol (3×10^{-10} mol cm⁻²),¹¹ which agree with experimental values at the same concentration. From eq 3, the values are as follows: $\Gamma_{\text{OH}} = 3 \times 10^{-10}$ mol cm⁻² and $\Gamma_{\text{O}_3} = 9 \times 10^{-10}$ mol cm⁻². Γ_{OH} is equivalent to that of ethanol, while Γ_{O_3} is 3 times larger. Although Γ_{O_3} is 3 times larger than Γ_{OH} at this aqueous concentration, O₃ is less soluble in water. The calculated value of c_g for O₃ is 3 orders of magnitude larger than that for OH with the same value of c_l . These calculations predict that the surface activity of OH and O₃ is similar to that of methanol and ethanol at the same aqueous concentration, although differences in the solubilities of these species mean that different gas-phase concentrations are needed to achieve the calculated surface excesses.

Experimental verification of the surface activity for OH and O₃ is necessary. One possibility is to monitor the change in surface tension of an aqueous solution in the presence of the gas-phase species relative to neat water. It is already known that the surface tension of water decreases with an increase in atmospheric pressure, which suggests that atmospheric gases, such as N₂ and O₂, adsorb to the surface.^{22,61} The possibility of obtaining surface selective electronic and vibrational spectra of these solutes in water also exists, although this represents a challenging task for a variety of reasons.⁶² Finally, in the case of OH, it may be possible to quantify its surface excess by isotopic substitution combined with neutron reflection, similar to a previous report for aqueous solutions of ethanol.⁶³

3. Solvation Structure and Interface Orientation. A comparison between the equilibrium aqueous solvation structure in the bulk and at the surface provides molecular-scale insight into the surface activity. The surfactant nature of amphiphilic molecules, such as methanol,⁶⁴ ethanol,⁶⁵ and dimethyl sulfoxide,⁶⁶ is attributed to segregation of the hydrophobic moiety from bulk water, while keeping the hydrophilic portion oriented with the respect to the adjacent to water so that the hydrogen bonding is maximized. Recent simulations by Petersen et al., using the multistate empirical valence bond method and classical MD, show that the hydronium ion is surface active for reasons analogous to those for amphiphiles.⁶⁷ The “hydrophobic” portion of hydronium is on the lone pair side of the oxygen, and at the interface, the ion is oriented such that this portion is pointing away from the liquid while three hydrogen bonds with water are maintained. It may be that concepts used to understand the solvation of amphiphilic surfactants are applicable to a broader group of molecules than previously thought.

Insight into the solvation of OH and O₃ is obtained by comparing the equilibrium aqueous solvation structure of each species in bulk water to that at the air–water interface. The O–O radial distribution functions (RDFs) of OH, O₃, and H₂O with liquid water in the bulk are compared in Figure 6A. For O₃, the central oxygen atom is used to calculate the RDF. Only

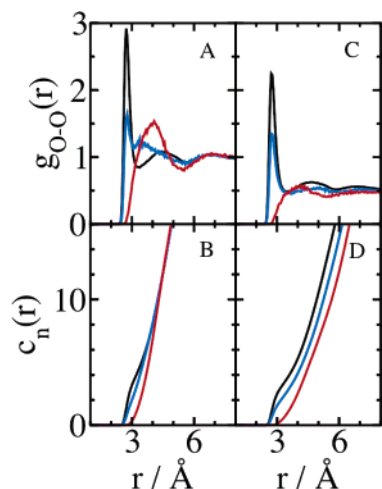


Figure 6. Solute–water radial distribution functions and running coordination numbers for OH (blue), O₃ (red), and H₂O (black): (A and B) bulk water and (C and D) air–water interface.

configurations in which the solute molecule is located in bulk water ($|z| < 7$ Å) are used to calculate these functions. The water structure around OH and O₃ is distinct from that of pure water when $r < 6$ Å, but it is identical to pure water at larger distances. This distance corresponds to the first two solvent shells in pure water. While the O₃ RDF exhibits the standard shape for a nonpolar solute, the OH RDF is bimodal with a narrow peak centered at $r = 2.8$ Å and another broad peak that extends over a 3 Å radial distance.

Further information about the solvation structure around OH and O₃ is provided by the running coordination number, $c_n(r)$, in the bulk liquid, which is shown in Figure 6B. These data show that the first peak in the OH RDF corresponds to two water molecules that are associated with OH. Visualization of configurations with OH located in bulk water shows that OH is acting as a hydrogen bond donor with one of these water molecules and as a hydrogen bond acceptor with the other water molecule, in agreement with the structures presented above for the OH(H₂O)_{*n*} clusters. The second peak in the OH RDF occurs at the first minimum of the pure water RDF, which results in the coordination number around OH and that around a water molecule being the same in bulk water when $r > 3.5$ Å.

It is interesting that the traditional picture of liquid solvent shells around a solute⁶⁸ must be modified for the OH radical in liquid water. This finding is also reported from Monte Carlo (MC)⁴⁴ and Car–Parrinello type molecular dynamics (CPMD)^{69–71} simulations of OH in bulk liquid water. The simulation methodology and parameters that yield the most accurate OH solvation structure in liquid water are yet to be elucidated, but it is clear that all of the simulations find that the removal of a single hydrogen atom from a water molecule to yield the OH radical results in a unique solvation structure that is significantly different from that of pure water. Although the detailed shape of the OH RDF from the MC simulation is different from the one shown in Figure 6A, both RDFs exhibit a bimodal peak with two maxima at $r \sim 2.7$ and 3.2 Å. This is attributed to two water molecules that are coordinated in a very specific orientation around OH. The *ab initio* molecular dynamics simulations based on the standard density functional theory (e.g., BLYP functional) yield qualitatively different O–O RDFs. However, these RDFs suffer from the known tendency of BLYP to overestimate the hemibonded structures. When a self-interaction correction is included in the density functional calculations,⁷¹ the hemibonded peak around 2.3 Å is no longer

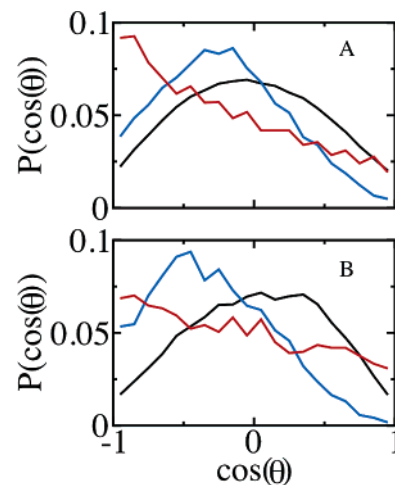


Figure 7. Probability distribution of the dipole orientation for OH (blue), O₃ (red), and H₂O (black) located in 1.8 Å surface layers at the air–water interface, as explained in the text: (A) surface layer nearest the bulk liquid and (B) surface layer nearest the gas phase.

present. Moreover, there is a qualitative agreement between the O–O RDF shown in Figure 6A and the RDF obtained from the self-interaction corrected simulation (in particular, the one employing the scaled self-interaction correction method proposed by VandeVondele and Sprik⁷¹). The high quality of the new OH force field parametrization (OH1) presented in this work is further supported by an additional result of the self-interaction corrected *ab initio* MD, namely, that the number of hydrogen bonds between the OH and the solvent water molecules in the bulk liquid is on average fewer than three, which is in agreement with the findings of our MD simulation employing the OH1 force field. It is also important to note that the O–O RDFs between aliphatic alcohols and water in bulk solution do not exhibit the unique shape observed for OH in water.^{72,73} Furthermore, O–O RDFs calculated from classical⁷⁴ and *ab initio*^{75,76} simulations of the hydroxide ion in bulk water exhibit a conventional shape. The currently available evidence suggests that the solvation structure around the OH radical is truly unique for a solute in a liquid near 300 K.

Rather than focus on the details of the solvation structure in the bulk liquid, the purpose of this discussion is to establish how the solvation structure differs at the air–water interface from the bulk liquid. In Figure 6C, the O–O RDFs for OH, O₃, and H₂O at the air–water interface are compared. These RDFs are calculated from equilibrium configurations where the solute molecule is located at the interface ($z_{90} < z < z_{10}$) and, therefore, approach a value of 0.5 at large distances. The RDF for OH at the air–water interface does not exhibit the same shape as OH in bulk water. In fact, its shape is similar to pure water, but there are fewer water molecules coordinated around OH at the interface than for pure water, as evidenced by the running coordination number shown in Figure 6D. It appears that OH is incorporated into the water structure better at the surface than in the bulk liquid. The O₃ RDF at the air–water interface exhibits a peak with a much smaller magnitude than in the bulk liquid and almost no solvation structure. Unlike that of the bulk liquid, the $c_n(r)$ values for OH and O₃ at the interface do not reach the value for H₂O since the bulk liquid density at larger distances does not compensate for the reduced level of solvation in the first shell.

In addition to the solvation structure, it is important to establish the solute orientation at the interface to gain an understanding of the surface activity. In Figure 7, the probability distributions of the OH, O₃, and H₂O orientations, $P[\cos(\theta)]$,

are shown for molecules in the top two molecular layers at the surface. The angle, θ , is between the electric dipole moment vector and the vector normal to the liquid surface, where the dipole moment vector corresponds to the bond vector for OH and the bisector of the angle for O₃ and H₂O. The vectors are defined such that the $\cos(\theta) = 1$ case corresponds to the dipole vector perpendicular to the surface plane with the positive pole pointing toward the vapor and the $\cos(\theta) = 0$ case corresponds to the dipole vector parallel to the surface plane. The lower and upper molecular layers are defined as follows: $z_{90} < z < z_{\text{GDS}}$ and $z_{\text{GDS}} < z < z_{10}$, respectively. Each layer is 1.8 Å wide in the z dimension.

$P[\cos(\theta)]$ values for OH, O₃, and H₂O in the bulk liquid are uniform (data not shown), as expected for an isotropic environment. The probability distributions of the H₂O dipole orientation are consistent with previously published results for the liquid–vapor interface of water described by the SPC/E model.⁷⁷ The most probable orientation of water dipoles in the layer nearest the bulk is nearly parallel to the surface with a slight tilt toward the bulk ($\theta = 95^\circ$). For water molecules in the upper surface layer, the dipole vector is most probably oriented nearly parallel to the surface, but with a slight tilt toward the vapor ($\theta = 78^\circ$).

The orientation of the OH dipole vector ranges from nearly parallel to the surface to perpendicular to the surface with the hydrogen atom pointing toward the bulk, which is consistent with the interface orientation predicted with the OH2 force field parameters¹⁹ and a nonpolarizable model.²² The perpendicular orientation of OH is slightly more pronounced in the upper surface layer than in the lower. The O₃ dipole in the lower surface layer is strongly oriented perpendicular to the surface with the side oxygen atoms pointing toward the vapor, but this becomes less pronounced and more uniformly distributed in the upper layer. In general, we find that OH and O₃ dipoles orient such that the positive pole is pointing toward the bulk liquid with a weak dependence on the local density. For these solutes, this orientation corresponds to the larger portion of the molecule pointing out of the liquid into the gas phase.

The solvation of any solute is governed by interplay between the solvent–solvent and solute–solvent interactions. In the case of OH and O₃, a more favorable balance between these two factors is found at the interface than in the bulk, as evidenced by the surface free energy minimum. With our data, the various contributions to solvation cannot be determined, but there are sufficient data to highlight features for future studies of this topic. The fact that OH and O₃ are both surface active, but have large differences in dipole magnitude and molecular size, indicates that both factors may be important. In the bulk liquid, the strongly dipolar nature of OH results in an ordering of a couple of water molecules, as evidenced by the O–O RDF, and disrupts its hydrogen bonding network. It appears that OH perturbs the water structure to a lesser degree at the surface. The water structure is also less likely to be perturbed by a weakly dipolar molecule that is the size of O₃ at the surface than in the bulk. Furthermore, OH and O₃ are oriented at the surface such that one portion is excluded from the liquid, which is similar to the case for amphiphilic molecules. A comprehensive list of the driving forces for surface activity may include the electronic distribution and molecular size, in addition to hydrophobicity. This is supported by the finding that halide anions are increasingly surface active as the size and polarizability increases.²⁶ Fully resolving the importance of different factors in determining surface activity is a difficult problem since the factors are difficult to separate from one another. This issue is reserved for future work. In the next section, the accom-

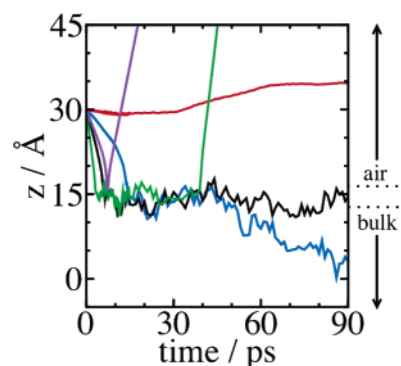


Figure 8. Possible outcomes for a gas-phase molecule approaching a liquid surface: absorption (blue), adsorption (black), desorption (green), scattering (purple), and deflection (red). The interface region is indicated by the horizontal dotted lines to the right of the panel.

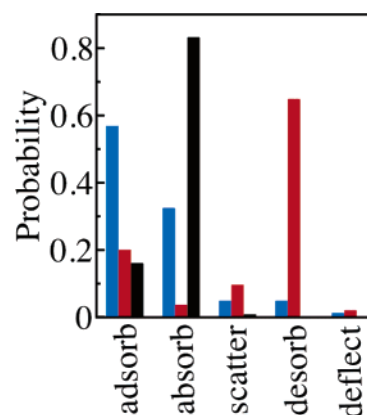


Figure 9. Probability of observing each possible outcome shown in Figure 4 for OH (blue), O₃ (red), and H₂O (black) approaching the surface of liquid water with a thermal impact velocity at 300 K.

modation of gas-phase OH and O₃ is described in the context of the free energy profiles, surface excesses, and solvation behavior presented above and compared to the accommodation of gas-phase H₂O.

C. Gas-Phase OH, O₃, and H₂O Accommodation. 1.

Characterization of the Overall Process. A gas-phase molecule with a thermal impact velocity approaching the surface of liquid water may undergo one of five different outcomes in tens of picoseconds. An example of each of these outcomes is depicted in Figure 8 by the position in the z dimension of an impinging molecule as a function of time. Scattering, desorption, and deflection result in the incident molecule returning to the gas phase. Deflection is observed when the assigned molecular center of mass z velocity is small and a repulsive interaction with the surface is sufficient to repel the molecule into the gas phase. Desorption is differentiated from scattering by a minimum residence time on the water surface prior to the return to the gas phase. Adsorption and absorption result in the incident molecule being located in the water slab, where adsorbed trajectories are at the interface and absorbed trajectories are in the bulk liquid.

The probability of observing each of the five possible outcomes for OH, O₃, and H₂O approaching the surface of liquid water at 300 K with a thermal impact velocity is shown in Figure 9. The outcomes are determined at the end of 90 ps trajectories. Note the sum of the probabilities for adsorption and absorption account for $\geq 90\%$ of the observed outcomes for OH and H₂O. This is in contrast to O₃, which is more likely to desorb from the surface than absorb into the bulk liquid. The data in Figure

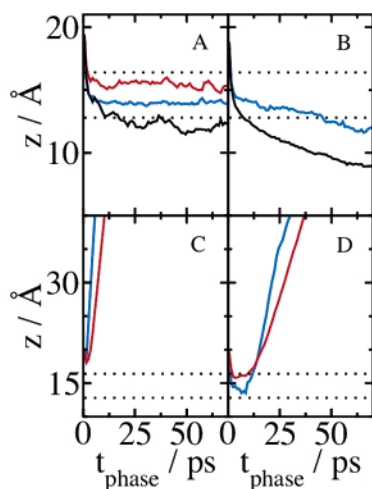


Figure 10. Time-dependent z position of incident OH (blue), O_3 (red), and H_2O (black) molecules averaged over trajectories that (A) adsorb, (B) absorb, (C) scatter, and (D) desorb. The dotted lines in each panel denote the air–water interface region.

9 are used in the following sections to determine thermal and mass accommodation coefficients.

A qualitative interpretation of the data in Figure 9 is made using the free energy profile for each species to be transferred from the gas phase to the bulk liquid (Figure 5). The OH radical is most likely located at the surface or in the bulk because the free energy minimum is near z_{90} . Desorption is unlikely due to a 4.2 kcal/mol increase in the free energy for this process. This is in contrast to O_3 , which is more likely to desorb since the free energy minimum occurs near z_{10} . Furthermore, the increase in free energy for O_3 desorption (1.2 kcal/mol) is less than that for absorption (1.8 kcal/mol). The free energy profile for water monotonically decreases from the gas phase to bulk water and does not exhibit a surface minimum.^{13,22,78} Therefore, absorption is the most probable outcome for impinging H_2O molecules. These results are consistent with the previous finding that the motion of an adsorbed ethanol molecule perpendicular to the surface is described by the one-dimensional diffusion equation in the presence of an external potential, the free energy profile.¹¹

Further characterization of the overall process is provided in Figure 10. Each panel shows the z position of the incident molecules averaged over a different outcome as a function of time. Only outcomes that compose $\geq 5\%$ of the total trajectories are shown. The time axis is denoted by t_{phase} because it corresponds to the amount of time after the incident molecule first passes below $z = 21$ Å, which is approximately 5 Å above the liquid surface. Since the molecules are assigned different velocities in the z dimension and, therefore, arrive at the liquid surface at different times, this definition is necessary to phase time-dependent results to a common initial point. Adsorbed OH and O_3 trajectories are located on average at a z position that corresponds to the location of the minimum in the free energy profile for transfer from the gas phase to the bulk liquid. Adsorbed H_2O molecules are near the dividing surface between the bulk liquid and the surface. Absorbed H_2O molecules readily enter bulk water, while OH enters more slowly since the free energy of solvation must increase by 1.1 kcal/mol.

The trajectories that scatter do so from a z position that corresponds to a density of $<10\%$ of bulk water and return to the gas phase nearly perpendicular to the surface. Desorbed trajectories leave the surface after a residence time on the surface, τ_{res} , which is defined by the time between first passing below $z = 21$ Å and going above $z = 25$ Å without returning

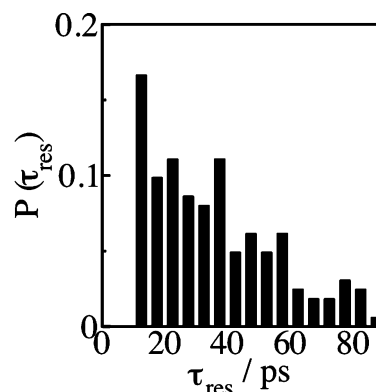


Figure 11. Probability distribution of residence times for O_3 trajectories that desorb from the air–water interface.

to the surface. The upper limit is selected on the basis of the fact that molecules that reach this distance always desorb from the surface in our simulations. In the case of O_3 , some of the molecules “hop” along the surface, where they begin to leave the surface only to be “sucked” back toward it, if their z position is <25 Å. The minimum value of τ_{res} observed for desorbed trajectories is 10 ps. While the data in Figure 10D suggest that the average τ_{res} is short, there is actually a broad distribution. The distribution of τ_{res} for the O_3 trajectories that desorb is shown in Figure 11, from which an average value of 36 ps is obtained. Further details are provided below on the kinetics and mechanisms of desorption and absorption.

2. Thermal Accommodation. The definition of the thermal accommodation coefficient, S , is given in eq 1. Prior to writing an expression for S determined from the simulation results, we must determine the outcomes that result in thermal equilibration of the incident molecule. This is accomplished by performing a detailed analysis of the time-dependent kinetic energy of the incident molecule according to the different outcomes. The function that is used to study the total time-dependent kinetic energy is given by^{11,21}

$$\delta KE_{\text{tot}}(t) = KE_{\text{tot}}(t) - \langle KE_{\text{tot}} \rangle \quad (5)$$

where $KE_{\text{tot}}(t)$ is the total kinetic energy of the incident molecule and $\langle KE_{\text{tot}} \rangle$ is the equilibrium ensemble average of the total kinetic energy. Furthermore, we take advantage of the fact that $\delta KE_{\text{tot}}(t)$ can be written as a sum of components

$$\delta KE_{\text{tot}}(t) = \delta KE_{\text{rot}}(t) + \delta KE_{\text{xtr}}(t) + \delta KE_{\text{ytr}}(t) + \delta KE_{\text{ztr}}(t) \quad (6)$$

to study the partitioning of the kinetic energy during the thermal accommodation process. In eq 6, the subscript rot represents the rotational kinetic energy and xtr, ytr, and ztr represent the translational kinetic energy in the x , y , and z dimensions, respectively. Each term in eq 6 is similar in form to that in eq 5, where the proper value for the equilibrium ensemble average is used depending on the component and the incident molecule.

The results of this kinetic energy analysis are shown in Figures 12–15. Each of these figures shows the average of $\delta KE_{\text{tot}}(t)$ and its four components over the trajectories of an incident molecule that result in a particular outcome. The incident molecule used to characterize the thermal accommodation of a particular outcome is the one that resulted in that outcome with the largest probability, which is representative of the time-dependent kinetic energy for the other molecules undergoing the same outcome. Therefore, the OH radical is selected for adsorption (Figure 12), H_2O for absorption (Figure

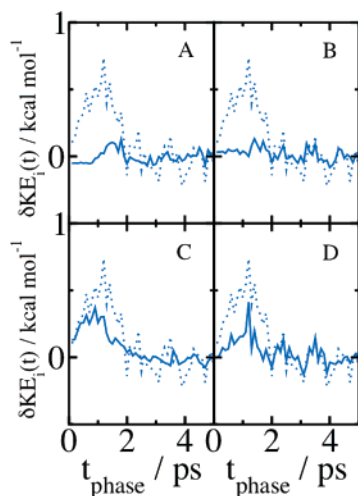


Figure 12. Time-dependent fluctuation from the equilibrium ensemble average of (A) *x* translational, (B) *y* translational, (C) *z* translational, and (D) rotational kinetic energy averaged over OH trajectories that adsorb. The dotted line in each panel corresponds to the total kinetic energy.

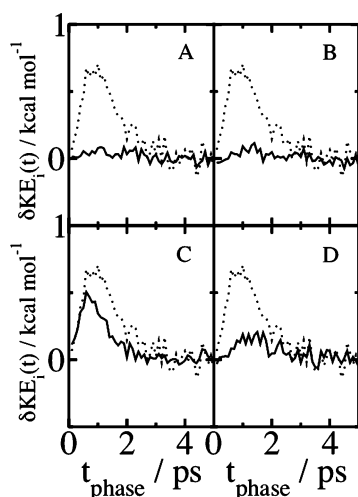


Figure 13. Time-dependent fluctuation from the equilibrium ensemble average of (A) *x* translational, (B) *y* translational, (C) *z* translational, and (D) rotational kinetic energy averaged over H₂O trajectories that adsorb. The dotted line in each panel corresponds to the total kinetic energy.

13), and O₃ for desorption (Figure 14). Both OH and O₃ trajectories are used to characterize scattering (Figure 15) since it is a low-probability event for both molecules. Since deflection is clearly not included in the calculation of *S*, only these four outcomes are considered. As in Figure 10, the time axis is denoted by t_{phase} so that the time-dependent kinetic energies are phased to a common initial point.

Regardless of the outcome, the incident molecule is accelerated toward the surface when it is approximately 5 Å above, as shown by the increase in the *z* translational kinetic energy from near zero when $t_{\text{phase}} = 0$. For trajectories that adsorb, absorb, or desorb, the thermal accommodation of the incident molecule occurs by a general process. This process is characterized by an increase in the total kinetic energy of the incident molecule to a maximum value that is approximately 0.5 kcal/mol larger than the equilibrium value. The initial rise is due mostly to the *z* translational kinetic energy, which is followed by a rotational excitation that is induced upon impact with the surface at $t_{\text{phase}} = 1$ ps. The excess kinetic energy is dissipated within approximately 2 ps of striking the surface, which is a general result

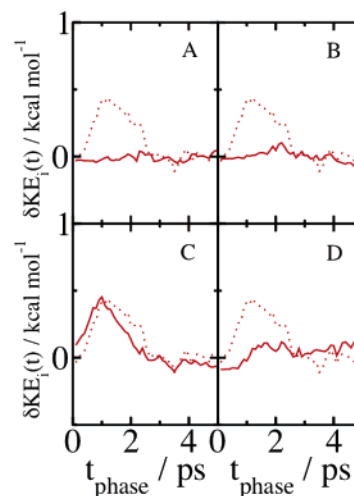


Figure 14. Time-dependent fluctuation from the equilibrium ensemble average of (A) *x* translational, (B) *y* translational, (C) *z* translational, and (D) rotational kinetic energy averaged over O₃ trajectories that desorb. The dotted line in each panel corresponds to the total kinetic energy.

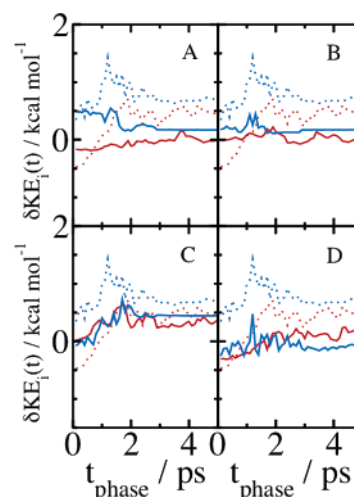


Figure 15. Time-dependent fluctuation from the equilibrium ensemble average of (A) *x* translational, (B) *y* translational, (C) *z* translational, and (D) rotational kinetic energy averaged over OH (blue) and O₃ (red) trajectories that scatter. The dotted line in each panel corresponds to the total kinetic energy.

based on similar analysis for ethanol, CO₂, and N₂.^{11,21} These results indicate that the process by which an incident molecule reaches thermal equilibrium is not correlated to its final outcome. This supports a description of the accommodation process by rapid thermal equilibration followed by diffusion on the solvation free energy profile in the *z* dimension, as discussed above in the interpretation of the data in Figure 9.

The O₃ and OH trajectories that do not reach thermal equilibrium with the liquid in approximately 2 ps scatter back into the gas phase. The total kinetic energy is approximately 0.5 kcal/mol above the equilibrium value when the scattered molecules leave the surface. This is mostly due to the *z* translational kinetic energy, which increases from the thermal value at $t_{\text{phase}} = 0$, but does not equilibrate. It is clear from the data in Figures 12–15 that the expression for *S* from the molecular dynamics simulations that is equivalent to eq 1 is given by

$$S = \frac{n_{\text{absorb}} + n_{\text{adsorb}} + n_{\text{desorb}}}{n_{\text{absorb}} + n_{\text{adsorb}} + n_{\text{desorb}} + n_{\text{scatter}}} \quad (7)$$

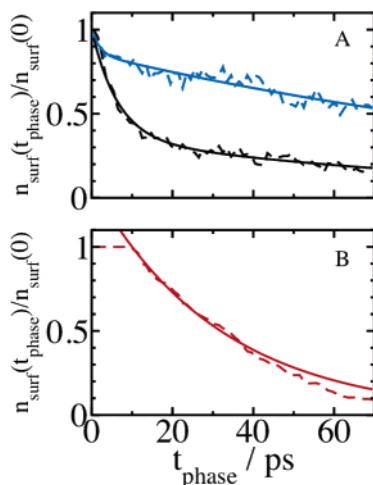


Figure 16. Normalized time-dependent surface population for (A) OH (blue) and H₂O (black) molecules that absorb and (B) O₃ molecules that desorb. For each molecule, the simulation data (---) and an exponential fit (—), as explained in the text, are shown.

where n_i represents the number of trajectories of an incident molecule that result in outcome i . The values of S determined from eq 7 for OH, O₃, and H₂O are 0.95, 0.90, and 0.99, respectively. These values indicate that nearly all of the collisions between thermal gas-phase molecules and a liquid surface result in “sticking”. An S value of 1 for H₂O on liquid water is inferred from experimental uptake measurements.⁷⁹ Furthermore, these values are consistent with trends observed in molecular beam experiments of several different gases impacting liquid glycerol or squalane with different collision energies,⁸⁰ which are supported by MD simulations of Ne and D₂O scattering from glycerol.^{81,82} At low experimental collision energies (~ 6 kJ/mol), the fraction of incident gases that thermalize is greater than 0.8. Also, as in the experimental results, we find a linear correlation between S and ΔG_s (data not shown) in the range of simulated solvation free energies. It does appear that this correlation is a general, empirical predictor for estimating S on a particular liquid.

3. Absorption and Desorption Kinetics. Another aspect of the accommodation process that can be studied using simulations is the kinetics of absorption and desorption. This information is crucial for establishing how the rates of absorption and desorption compare to the rate of thermal accommodation. Using MD simulations, Somasundaram et al. show that the surface lifetimes for adsorbed CO₂ (15.5 ps) and N₂ (3.3 ps) are sufficiently longer than the kinetic energy relaxation time (0.3–0.4 ps).²¹ Furthermore, the kinetic information provides insight into the mechanism by which a molecule located at a liquid surface is transferred to the bulk liquid or the gas phase.

In Figure 16, the normalized time-dependent surface population of OH and H₂O molecules that absorb (top panel) and O₃ molecules that desorb (bottom panel) is shown. The time axis is denoted by t_{phase} , which results in functions that decay from unity at $t_{\text{phase}} = 0$ to zero at $t_{\text{phase}} = \infty$. Depletion of the surface populations due to absorption is poorly described by a single-exponential decay, but is described well by a double-exponential function of the form

$$\frac{n_{\text{surf}}(t_{\text{phase}})}{n_{\text{surf}}(0)} = A \exp(-t_{\text{phase}}/\tau_A) + (1 - A) \exp(-t_{\text{phase}}/\tau_B) \quad (8)$$

where $n_{\text{surf}}(t_{\text{phase}})$ is the time-dependent number of adsorbed molecules that eventually absorb. The double-exponential fits

TABLE 5: Parameters for Double-Exponential Fits to the Time Evolution of the Surface Population

| molecule | A | τ_A (ps) | τ_B (ps) | τ_{absorb} (ps) |
|------------------|------|---------------|---------------|-----------------------------|
| OH | 0.14 | 2.0 | 150 | 130 |
| H ₂ O | 0.64 | 6.4 | 100 | 40 |

are also shown in Figure 16A for OH and H₂O. The total relaxation time for absorption is given by

$$\tau_{\text{absorb}} = A\tau_A + (1 - A)\tau_B \quad (9)$$

The parameters that yield the best fit to the simulation data shown in Figure 16A and the corresponding values of τ_{absorb} are given in Table 5.

From the data in Table 5, it is evident that there are two time components for the transfer of surface molecules to the bulk liquid, a short time component on the order of several picoseconds and a long time component on the order of hundreds of picoseconds. The value of τ_{absorb} for OH is greater than that for H₂O by a factor of 3.3. It appears that the two time components are characteristic of the absorption process, but are subject to modification by features of the solvation free energy profile in the z dimension. In the case of the OH radical, the 1.1 kcal/mol increase in the free energy for transfer from the surface minimum to the bulk liquid suppresses the rapid entry relative to H₂O, which does not exhibit a surface minimum.^{13,22,78}

When the values of τ_A in Table 5 are compared to the time scale for thermal accommodation, it is evident that a fraction of the incident molecules are absorbing while the excess kinetic energy is being dissipated. The data in Figure 13 show that the dissipation of excess kinetic energy is complete at $t_{\text{phase}} = 3$ ps. By this time, 11% of the OH radicals and 14% of the H₂O molecules that absorb within 90 ps are located in the bulk liquid. The absorption of a small fraction of the incident molecules while thermal accommodation is occurring may be the reason for the double-exponential decay of the surface populations in Figure 16A. This conclusion is supported by the results for O₃ desorption kinetics in Figure 16B.

The O₃ surface population does not decrease for $t_{\text{phase}} < 10$ ps because this is the minimum residence time that is observed for desorbed trajectories. The minimum residence time is a sufficient length of time for thermal equilibration, which is complete by $t_{\text{phase}} = 3$ ps, as shown in Figure 15. Since desorption does not occur until after thermal equilibration is complete, the data in Figure 16B are reasonably well described by a single-exponential decay with a time constant of 32 ps. This is consistent with the average residence time ($\tau_{\text{res}} = 36$ ps) determined for desorbed O₃ trajectories from the distribution in Figure 11.

4. Predicting Mass Accommodation Coefficients from MD Simulations. As discussed in the Introduction, α is a parameter in a phenomenological model of gas-phase uptake, the resistor model.⁹ For the case of nonreactive uptake considered in this paper, the resistor model describes the time-dependent uptake, $\gamma(t)$, in terms of the rates of gas and liquid transport, $\gamma_{\text{gas}}(t)$ and $\gamma_{\text{liq}}(t)$, respectively, and α

$$\frac{1}{\gamma(t)} = \frac{1}{\gamma_{\text{gas}}(t)} + \frac{1}{\gamma_{\text{liq}}(t)} + \frac{1}{\alpha} \quad (10)$$

The determination of α from MD simulations is not a straightforward problem. It is complicated by the fact that the fate of adsorbed molecules is not clearly determined within currently accessible simulation times. These molecules may

diffuse into the bulk liquid or desorb into the gas phase over a period of time longer than the length of the simulations. However, the outcomes of the adsorbed trajectories can be predicted on a theoretical basis and included in the calculation of α .

There are several molecular interpretations of α . One of these is as a probability that a molecule striking a liquid surface is solvated in the liquid

$$\alpha = \frac{\text{number of impinging molecules solvated in the liquid}}{\text{number of molecules impinging on liquid surface}} \quad (11)$$

This interpretation is ambiguous because of the finite lifetime of molecules that are thermally accommodated and surface active. Adsorbed molecules are problematic because they should be observed for a sufficiently long period of time so that their fates are determined. If adsorbed trajectories contribute to the uptake, then an upper limit to the value of α , α_{upper} , is determined directly from the MD simulations

$$\alpha_{\text{upper}} = \frac{n_{\text{absorb}} + n_{\text{adsorb}}}{n_{\text{adsorb}} + n_{\text{absorb}} + n_{\text{desorb}} + n_{\text{scatter}}} \quad (12)$$

The value of α_{upper} depends on the length of the trajectories. Therefore, this value needs to be corrected using a factor that accurately accounts for the ultimate fate of adsorbed trajectories.

Wilson and Pohorille provide an estimate for the correction factor based on the free energy profile for transfer of the solute molecule from the gas phase to the bulk liquid.¹¹ This correction factor, $p_{\Delta G}$, is given by

$$p_{\Delta G} = \frac{e^{-\beta \Delta G_{s \rightarrow g}}}{e^{-\beta \Delta G_{s \rightarrow l}}} \quad (13)$$

where $\Delta G_{s \rightarrow g}$ is the free energy difference for transfer from the surface to the gas phase and $\Delta G_{s \rightarrow l}$ is the free energy difference for transfer from the surface to the bulk liquid. This represents the probability that an adsorbed molecule will desorb into the gas phase versus absorb into the bulk liquid. Negligible correction factors are obtained in the case of ethanol¹¹ and water¹⁷ accommodation due to much larger increases in the free energy for desorption from the surface relative to absorption.

A problem with $p_{\Delta G}$ is that it does not exhibit the correct range of values. To correct the value of α for the long-time behavior of the adsorbed trajectories, the value of $p_{\Delta G}$ should be limited to the range between 0 and 1. In fact, this is not the case for $p_{\Delta G}$, which may result in a prediction for α that is also outside its range between 0 and 1. This is the case for O_3 if one uses this analysis to determine α . A correction factor is reported in our recent communication that overcomes the limitations of eq 13.¹⁸ It is calculated directly from the accommodation trajectories and produces values of α in the correct range. It is analogous to another molecular interpretation for α , given by

$$\alpha = \frac{k_{\text{absorb}}}{k_{\text{absorb}} + k_{\text{desorb}}} \quad (14)$$

where k_{absorb} and k_{desorb} are the rate constants for absorption and desorption, respectively.⁹ This expression is valid if one assumes a unit probability of sticking ($S = 1$) and rapid thermal accommodation relative to absorption and desorption. The validity of these assumptions is supported by the results and discussion presented above for thermal accommodation and the kinetics of absorption and desorption. Essentially, it represents the probability that a thermally accommodated molecule diffuses

TABLE 6: Mass Accommodation Coefficients for OH, O_3 , and H_2O

| molecule | p_k | α |
|----------------------|-------|----------|
| OH | 0.87 | 0.83 |
| O_3 | 0.053 | 0.047 |
| H_2O | 1.0 | 0.99 |

into the bulk solution rather than desorb into the gas phase. The correction factor, p_k , predicts the number of adsorbed trajectories that dissolve into the bulk liquid at a later time using the expression

$$p_k = \frac{n_{\text{absorb}}}{n_{\text{absorb}} + n_{\text{desorb}}} \quad (15)$$

The mass accommodation coefficient is then written as

$$\alpha = \frac{n_{\text{absorb}} + p_k n_{\text{adsorb}}}{n_{\text{adsorb}} + n_{\text{absorb}} + n_{\text{desorb}} + n_{\text{scatter}}} \quad (16)$$

The values of p_k and α for OH, O_3 , and H_2O are listed in Table 6.

The α values for OH and O_3 in Table 6 are different from the corresponding values obtained with previous force fields for OH and O_3 ¹⁹ that are revised in this work. The original force fields for OH (OH2) and O_3 (OZ3) predict mass accommodation values of 0.26 and 0.008, respectively. The free energy profiles corresponding to these force fields predict a less favorable solvation free energy than the revised force fields and, therefore, predict smaller α values. We note that the revised force fields predict solvation free energies that are in better agreement with the experimental values than the original force fields, which provides confidence in the values reported in Table 6. The sensitivity of the solvation free energy profile and α to the force field parameters highlights the importance of solute force field development in this type of study.

The α values predicted from simulations are compared to those determined from experiments. Experimental values of α for OH, O_3 , and H_2O are ~ 0.004 ,^{83,84} 0.04,⁸⁵ and 0.2,⁷⁹ respectively. The experimental reference cited for O_3 shows that various groups measure α in a range from 0.00053 to 0.1 at similar temperatures.⁸⁵ The values for OH and H_2O do not agree with those in Table 6, while that for O_3 is within the range of experimentally measured values. However, we consider the agreement in the case of O_3 to be fortuitous since α is near zero and since poor agreement with experiments is obtained for OH and H_2O . The source of disagreement between simulations and experiments is not clear. The simulations test whether molecular interpretations of experimental α values are valid, assuming that the potentials are sufficiently accurate to describe this process. Our results suggest that the molecular interpretations given in eqs 11 and 14 are not valid. However, it is not evident that one should expect quantitative agreement. There is a large gap in the spatiotemporal scale that must be bridged in going from the molecular simulations to uptake experiments. Simulations on the nanometer length and picosecond time scales may not correspond to experimental uptake measurements being made with micron-sized systems on the microsecond to millisecond time scale due to additional physical processes occurring in the experimental systems that are not captured in the simulations. Since these issues complicate the comparison of α determined from experiments and simulations and are yet to be resolved, it is difficult to assess the accuracy of the resistor model in modeling gas-phase uptake. Rather, the remainder of

this paper is focused on comparing the various formulations of the accommodation process.

5. Formulations of Gas-Phase Accommodation. The mechanism by which a gas-phase molecule is incorporated into a liquid is a fundamental process in physical chemistry with significance not only with respect to uptake but also with respect to condensation and evaporation. By comparison of the current formulations using the simulation data, molecular level detail that is relevant to the uptake process, and not available from experiments, may provide necessary insight for modifying the existing formulations so that they are in agreement with one another.

One formulation that is derived from experimental results is based on nucleation theory.⁹ In this formulation, the interface region is considered to be an association of clusters of various sizes that are constantly forming and falling apart. An incident gas-phase molecule can adsorb to a cluster and eventually be solvated in the bulk liquid if the cluster is greater than a critical size, N^* , which includes the incident molecule. There is an entropic barrier to forming clusters of the critical size, where those that do not fall apart. This can be reinterpreted in terms of a capillary wave model, where the coordination number replaces the cluster size and uptake occurs via progressive absorption into a mobile liquid surface.¹⁰

There are several issues regarding the physical description of the accommodation process according to nucleation theory that we wish to address. Describing the gas–liquid interface as a region containing clusters of various sizes in the vicinity of the liquid surface contradicts the conventional description of interface structure. Liquid surfaces are corrugated due to capillary fluctuations, but are molecularly sharp with an abrupt, well-defined transition from the bulk liquid to the gas phase.^{60,86} If nucleation theory provides an accurate physical description of the uptake process, then there should be evidence of a barrier to critical cluster formation in the simulations.

If a barrier exists to formation of a critical cluster in gas-phase accommodation, what should the time-dependent cluster size look like? The incoming molecule samples configurations in which the cluster size is less than N^* until there is sufficient free energy to overcome the barrier to forming a critical cluster. The experimental value of N^* from the nucleation model for the uptake of water is 1.7,⁷⁹ and the range of values reported for various gas-phase molecules is approximately 1.5–3.⁹ Apparently, N^* is related to the molecular structure, where incident molecules that form multiple hydrogen bonds with water exhibit an N^* smaller than the values of those that form fewer hydrogen bonds. If a significant barrier to forming N^* is not present, then the cluster size is expected to progressively increase as the molecule approaches the surface and, subsequently, adsorbs.

The results from a preliminary investigation of time-dependent cluster size are shown in Figure 17, where the cluster size, N , is interpreted to be the incident molecule plus the number of solvent water molecules that are within a distance that corresponds to the first minimum of $g_{O-O}(r)$ at the air–water interface (Figure 6C), which are 3.5, 5.4, and 3.5 Å for OH, O₃, and H₂O, respectively. The equilibrium values of N , N_{equ} , at these distances are 3.6, 9.6, and 4.7 for OH, O₃, and H₂O, respectively. Figure 17 shows the time-dependent function given by

$$C_N(t_{\text{phase}}) = \frac{N(t_{\text{phase}}) - N_{\text{equ}}}{N(0) - N_{\text{equ}}} \quad (17)$$

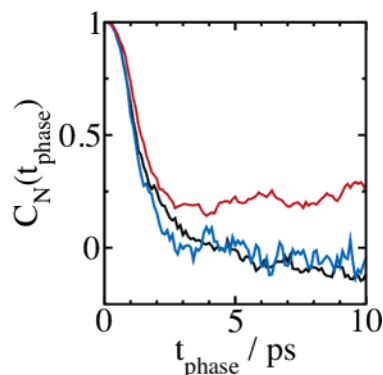


Figure 17. Normalized time-dependent fluctuation from the equilibrium coordination number in the first solvent shell for OH trajectories that adsorb (blue), O₃ trajectories that desorb (red), and H₂O trajectories that adsorb (black).

for OH radicals that adsorb, O₃ molecules that desorb, and H₂O molecules that adsorb. This function is used because it allows for a comparison of the time scales for approaching equilibrium solvation at the air–water interface for molecules with different N_{equ} values.

$C_N(t_{\text{phase}})$ rapidly decreases as the incident molecule is solvated at the interface at a rate that is not strongly dependent on the incident molecule or the outcome. This suggests that there is not a significant barrier to solvation around the incident molecule and that there is a characteristic time scale for this process. OH and H₂O reach N_{equ} within 2–3 ps of striking the surface at $t_{\text{phase}} = 1$ ps. For H₂O, $C_N(t_{\text{phase}})$ reaches a negative value since these trajectories absorb into the bulk liquid. O₃ does not reach N_{equ} within the 10 ps before desorption begins. This is attributed to the fact that some of the O₃ molecules can hop along the surface before desorbing, where temporary excursions into the region above the liquid surface result in a smaller value of $N(t_{\text{phase}})$ than N_{equ} . Recall that these molecules are also thermally excited until approximately $t_{\text{phase}} = 3$ ps, which is the time at which $C_N(t_{\text{phase}})$ stops decreasing and exhibits asymptotic behavior. There is a direct correlation between the time scales for dissipation of excess kinetic energy and the decrease in $C_N(t_{\text{phase}})$. During the acceleration of the incident molecule toward the surface and for 2 ps after striking the surface, when the molecule is dissipating excess kinetic energy to the solvent, $C_N(t_{\text{phase}})$ is decreasing. Once the molecule reaches thermal equilibrium, $C_N(t_{\text{phase}})$ stops decreasing and the value it reaches is representative of the final fate of the trajectory.

The behavior of the time-dependent coordination number supports the formulation for gas-phase uptake at a liquid surface developed by Knox and Phillips that is based on capillary wave theory.¹⁰ The coordination number progressively increases on a time scale of several picoseconds while thermal accommodation is occurring. Although the data in Figure 17 do not appear to support the nucleation model for gas-phase accommodation, more extensive calculations are planned for the future since classical simulations do not necessarily model certain aspects of nucleation accurately.⁸⁷ To make greater contact with the nucleation model, we plan on calculating the free energy, not as a function of the distance from the center of the slab but rather as a function of N . This may help to resolve the discrepancy between formulations for gas-phase uptake from macroscopic experiments and molecular simulations. It may also be useful to investigate other reaction coordinates for this process that are not currently being considered.

IV. Conclusions

The results of *ab initio* calculations and MD simulations of the equilibrium aqueous solvation and gas-phase accommodation of OH and O₃ on liquid water at 300 K are presented. Polarizable force fields for OH and O₃ are developed that agree with experimental hydration free energies and the geometries and energies of small clusters from *ab initio* calculations. The free energy profiles for the transfer of OH and O₃ from the gas phase to bulk water exhibit surface minima, but not a barrier to solvation in the bulk liquid from the surface-adsorbed state. The magnitudes of the surface minima are such that the calculated surface excesses are similar to those of other well-known surfactants, such as methanol and ethanol. Like other surfactants, OH and O₃ exhibit a preferential orientation at the surface. A comparison of the solvation structure at the air–water interface to the bulk liquid suggests that these solutes are incorporated into the water structure better at the surface.

A molecular perspective of gas-phase accommodation is also provided. S and α are determined for OH, O₃, and H₂O on liquid water at 300 K. A correction for α is used that accounts for the eventual fate of molecules adsorbed at the air–water interface. Following acceleration toward the liquid surface, which begins when the incident molecule is approximately 5 Å above it, the dissipation of excess kinetic energy occurs within approximately 2 ps of striking the surface for molecules that stick. The time scales for absorption and desorption, which are on the order of tens to hundreds of picoseconds, are much longer than that for thermal equilibration. The accommodation can be approximately treated as a two-step process consisting of first reaching thermal equilibrium followed by absorption or desorption. However, there is a correlation between incident molecules that are not at thermal equilibrium and rapid absorption into the bulk liquid. Scattering is a low-probability event that occurs when molecules do not reach thermal equilibrium within 2 ps of striking the surface. The probability of scattering is correlated with the hydration free energy.

An investigation of the time-dependent coordination number shows that the growth of the solvation structure around the incident molecule occurs while the excess kinetic energy is being dissipated. Evidence of a barrier to forming a critical cluster size is not found, and in fact, a characteristic time scale for this process is observed that is independent of the incident molecule and the eventual outcome of the trajectory. This supports a model for the accommodation process that is described by a low probability of scattering and a rapid increase in the coordination number while thermal equilibration is occurring. Following equilibration, the remainder of the process is described by diffusion perpendicular to the surface governed by the free energy profile.

The nature of the discrepancy between experimental α values extracted from the resistor model and the values reported here is still not clear. Molecular dynamics simulations do not support molecular interpretations of experimental α values. Usage of experimental α values in the nucleation model leads to the prediction of a significant free energy barrier to cluster formation at the liquid surface. Evidence of this barrier is not observed in the simulations for a reaction coordinate based on the distance from the center of the aqueous slab or the coordination number, although a more extensive investigation of the latter reaction coordinate is planned for future work.

Given that accurate, polarizable intermolecular potentials have been developed for OH and O₃, they can be used to further develop our understanding of why these solutes, and other small, atmospheric gases, exhibit a free energy minimum for surface

solvation. Furthermore, these potentials are useful for classical simulations in cluster and extended aqueous slab systems where the polarizability is an important feature for making accurate predictions of structure, spectra, and dynamics, particularly at liquid surfaces and in systems containing ions.

V. Atmospheric Chemistry Implications

The calculations reported in this work indicate that two important atmospheric oxidants, OH and O₃, exhibit surface excesses in liquid water. Therefore, one may expect an excess number of these oxidants at the air–water interface relative to the bulk liquid, and this is potentially important for heterogeneous reactions occurring in the atmosphere.^{18,22} The propensity of these two oxidants for the air–water interface combined with the presence of another species that can be oxidized at the surface of aerosol particles and fog or cloud droplets may be important for understanding the mechanisms of atmospheric processing of many organic and inorganic species. Examples of such heterogeneous processes include the oxidation of chloride and bromide ions by OH and O₃, respectively, in the presence of deliquesced NaCl and NaBr particles,^{4,6} oxidation of methanol to formaldehyde observed in field measurements of cloud droplets interacting with a plume from biomass burning,⁸⁸ and oxidation of anthracene adsorbed at the surface of water⁸⁹ or aqueous solutions containing alcohols or acids⁹⁰ upon exposure to gas-phase O₃.

The actual role that the surface excess of OH and O₃ plays in a particular reaction depends on a number of factors, including particle size, the reaction kinetics, and the potential surface excess of the species that is oxidized. In general, the relative importance of surface reactions is likely to increase for smaller particles with a large surface-to-volume ratio, for less volatile reactants, and for fast chemical reactions that occur before the oxidant absorbs or desorbs. The rapid thermal accommodation of OH and O₃ that occurs with a high probability coupled with time scales for absorption and desorption that range from tens to hundreds of picoseconds indicates that heterogeneous reaction mechanisms, such as the Langmuir–Hinshelwood mechanism,^{89,90} are useful for understanding oxidation processes at the air–water interface. Although the importance of atmospheric reactions occurring at the surface of aqueous aerosols is an open issue, the surface excess of OH and O₃ and its consequences for heterogeneous processes should be considered in tropospheric models and when interpreting the results of field measurements and laboratory experiments.

Acknowledgment. The University of California group is supported by grants from the National Science Foundation (CHE-0209719 and CHE-0431512). M.R. gratefully acknowledges support via Grant 1P05ME798 from the Ministry of Education of the Czech Republic. The funding of the Center for Biomolecules and Complex Molecular Systems is provided by the Ministry of Education of Czech Republic under the project number LC05A57. The work performed at the Institute of Organic Chemistry and Biochemistry of the Academy of Sciences of the Czech Republic was a part of the research project Z40550506. Part of the work was performed at Pacific Northwest National Laboratory under the auspices of the Division of Chemical Sciences, Office of Basic Energy Sciences, U.S. Department of Energy. We are grateful for discussions with Dr. Charles Kolb, Prof. John Hemminger, and Dr. Chris Knox during the preparation of the manuscript.

References and Notes

- (1) Finlayson-Pitts, B. J.; Pitts, J. N. *Chemistry of the Upper and Lower Atmosphere: Theory, Experiments, and Applications*; Academic Press: San Diego, 2000.
- (2) Mauldin, R. L.; Tanner, D. J.; Eisele, F. L. *J. Geophys. Res.* **1999**, *104*, 5817.
- (3) Kleinman, L. I.; Daum, P. H.; Lee, Y.-N.; Nunnermacker, L. J.; Springston, S. R.; Weinstein-Lloyd, J.; Rudolph, J. *J. Geophys. Res.* **2005**, *110*, doi: 10.1029/2004JD005096.
- (4) Knipping, E. M.; Lakin, M. J.; Foster, K. L.; Jungwirth, P.; Tobias, D. J.; Gerber, R. B.; Dabdub, D.; Finlayson-Pitts, B. J. *Science* **2000**, *288*, 301.
- (5) Laskin, A.; Gaspar, D. J.; Wang, W.; Hunt, S. W.; Cowin, J. P.; Colson, S. D.; Finlayson-Pitts, B. J. *Science* **2003**, *301*, 340.
- (6) Hunt, S. W.; Roeselova, M.; Wang, W.; Wingen, L. M.; Knipping, E. M.; Tobias, D. J.; Dabdub, D.; Finlayson-Pitts, B. J. *J. Phys. Chem. A* **2004**, *108*, 11559.
- (7) Gershenzon, M.; Davidovits, P.; Jayne, J. T.; Kolb, C. E.; Worsnop, D. R. *J. Phys. Chem. A* **2001**, *105*, 7031.
- (8) Nathanson, G. M.; Davidovits, P.; Worsnop, D. R.; Kolb, C. E. *J. Phys. Chem.* **1996**, *100*, 13007.
- (9) Kolb, C. E.; Davidovits, P.; Jayne, J. T.; Shi, Q.; Worsnop, D. R. *Prog. React. Kinet. Mech.* **2002**, *27*, 1.
- (10) Knox, C. J. H.; Phillips, L. F. *J. Phys. Chem. B* **1998**, *102*, 8469.
- (11) Wilson, M. A.; Pohorille, A. *J. Phys. Chem. B* **1997**, *101*, 3130.
- (12) Taylor, R. S.; Ray, D.; Garrett, B. C. *J. Phys. Chem. B* **1997**, *101*, 5473.
- (13) Taylor, R. S.; Garrett, B. C. *J. Phys. Chem. B* **1999**, *103*, 844.
- (14) Morita, A. *Chem. Phys. Lett.* **2003**, *375*, 1.
- (15) Morita, A.; Kanaya, Y.; Francisco, J. S. *J. Geophys. Res.* **2004**, *109*, doi: 10.1029/2003JD004240.
- (16) Morita, A.; Sugiyama, M.; Kameda, H.; Koda, S.; Hanson, D. R. *J. Phys. Chem. B* **2004**, *108*, 9111.
- (17) Vieceli, J.; Roeselova, M.; Tobias, D. J. *Chem. Phys. Lett.* **2004**, *393*, 249.
- (18) Roeselova, M.; Vieceli, J.; Dang, L. X.; Garrett, B. C.; Tobias, D. J. *J. Am. Chem. Soc.* **2004**, *126*, 16308.
- (19) Roeselova, M.; Jungwirth, P.; Tobias, D. J.; Gerber, R. B. *J. Phys. Chem. B* **2003**, *107*, 12690.
- (20) Somasundaram, T.; Lynden-Bell, R. M.; Patterson, C. H. *Phys. Chem. Chem. Phys.* **1999**, *1*, 143.
- (21) Somasundaram, T.; in het Panhuis, M.; Lynden-Bell, R. M.; Patterson, C. H. *J. Chem. Phys.* **1999**, *111*, 2190.
- (22) Vacha, R.; Slavicek, P.; Mucha, M.; Finlayson-Pitts, B. J.; Jungwirth, P. *J. Phys. Chem. A* **2004**, *108*, 11573.
- (23) Sugiyama, M.; Koda, S.; Morita, A. *Chem. Phys. Lett.* **2002**, *362*, 56.
- (24) Morita, A.; Sugiyama, M.; Koda, S. *J. Phys. Chem. A* **2003**, *107*, 1749.
- (25) Hanson, D. R.; Sugiyama, M.; Morita, A. *J. Phys. Chem. A* **2004**, *108*, 3739.
- (26) Jungwirth, P.; Tobias, D. J. *J. Phys. Chem. B* **2002**, *106*, 6361.
- (27) Jungwirth, P.; Tobias, D. J. *J. Phys. Chem. B* **2001**, *105*, 10468.
- (28) Salvador, P.; Curtis, J. E.; Tobias, D. J.; Jungwirth, P. *Phys. Chem. Chem. Phys.* **2003**, *5*, 3752.
- (29) Jungwirth, P.; Curtis, J. E.; Tobias, D. J. *Chem. Phys. Lett.* **2003**, *367*, 704.
- (30) Caldwell, J. W.; Kollman, P. A. *J. Phys. Chem.* **1995**, *99*, 6208.
- (31) Frisch, M. J.; Trucks, G. W.; Schlegel, H. B.; Scuseria, G. E.; Robb, M. A.; Cheeseman, J. R.; Zakrzewski, V. G.; Montgomery, J. A.; Stratmann, R. E.; Burant, J. C.; Dapprich, S.; Millam, J. M.; Daniels, A. D.; Kudin, K. N.; Strain, M. C.; Farkas, O.; Tomasi, J.; Barone, V.; Cossi, M.; Cammi, R.; Mennucci, B.; Pomelli, C.; Adamo, C.; Clifford, S.; Ochterski, J.; Petersson, G. A.; Ayala, P. Y.; Cui, Q.; Morokuma, K.; Malick, D. K.; Rabuck, A. D.; Raghavachari, K.; Foresman, J. B.; Cioslowski, J.; Ortiz, J. V.; Stefanov, B. B.; Liu, G.; Liashenko, A.; Piskorz, P.; Komaromi, I.; Gomperts, R.; Martin, R. L.; Fox, D. J.; Keith, T.; Al-Laham, M. A.; Peng, C. Y.; Nanayakkara, A.; Gonzalez, C.; Challacombe, M.; Gill, P. M. W.; Johnson, B. G.; Chen, W.; Wong, M. W.; Andres, J. L.; Head-Gordon, M.; Replogle, E. S.; Pople, J. A. *Gaussian 98*, revision A.11; Gaussian, Inc.: Pittsburgh, PA, 1998.
- (32) Case, D. A.; Pearlman, D. A.; Caldwell, J. W.; Cheatham, T. E.; Ross, W. S.; Simmerling, C. L.; Darden, T. A.; Merz, K. M.; Stanton, R. V.; Cheng, A. L.; Vincent, J. J.; Crowley, M.; Ferguson, D. M.; Radmer, R. J.; Seibel, G. L.; Singh, U. C.; Weiner, P. K.; Kollman, P. A. *AMBER 5*; University of California: San Francisco, 1997.
- (33) Ciccotti, G.; Ferrario, M.; Hynes, J. T.; Kapral, R. *Chem. Phys.* **1989**, *129*, 241.
- (34) Pearlman, D. A.; Case, D. A.; Caldwell, J. W.; Seibel, G. L.; Singh, U. C.; Weiner, P. K.; Kollman, P. A. *AMBER 4*; University of California: San Francisco, 1991.
- (35) Case, D. A.; Pearlman, D. A.; Caldwell, J. W.; Cheatham, T. E.; Ross, W. S.; Simmerling, C. L.; Darden, T. A.; Merz, K. M.; Stanton, R. V.; Cheng, A. L.; Vincent, J. J.; Crowley, M.; Tsui, V.; Radmer, R. J.; Duan, Y.; Pitera, J.; Massova, I.; Seibel, G. L.; Singh, U. C.; Weiner, P. K.; Kollman, P. A. *AMBER 6*; University of California: San Francisco, 1999.
- (36) Essmann, U.; Perera, L.; Berkowitz, M. L.; Darden, T.; Lee, H.; Pedersen, L. G. *J. Chem. Phys.* **1995**, *103*, 8577.
- (37) Vesely, F. J. *J. Comput. Phys.* **1977**, *24*, 361.
- (38) Ahlstrom, P.; Wallqvist, A.; Engstrom, S.; Jonsson, B. *Mol. Phys.* **1989**, *68*, 563.
- (39) Ryckaert, J. P.; Ciccotti, G.; Berendsen, H. J. C. *J. Comput. Phys.* **1977**, *23*, 327.
- (40) Berendsen, H. J. C.; Postma, J. P. M.; van Gunsteren, W. F.; DiNola, A.; Haak, J. R. *J. Chem. Phys.* **1984**, *81*, 3684.
- (41) Hirschfelder, J. O.; Curtiss, C. F.; Bird, R. B. *Molecular Theory of Gases and Liquids*; John Wiley & Sons: New York, 1964.
- (42) Karna, S. P. *Int. J. Quantum Chem.* **1998**, *70*, 771.
- (43) Jungwirth, P.; Tobias, D. J. *J. Phys. Chem. A* **2002**, *106*, 379.
- (44) Cabral do Couto, P.; Guedes, R. C.; Costa Cabral, B. J.; Martinho Simoes, J. A. *J. Chem. Phys.* **2003**, *119*, 7344.
- (45) Hamad, S.; Lago, S.; Mejias, J. A. *J. Phys. Chem. A* **2002**, *106*, 9104.
- (46) Cooper, P. D.; Kjaergaard, H. G.; Langford, V. S.; McKinley, A. J.; Quickenden, T. I.; Schofield, D. P. *J. Am. Chem. Soc.* **2003**, *125*, 6048.
- (47) Wang, B.; Hou, H.; Gu, Y. *Chem. Phys. Lett.* **1999**, *303*, 96.
- (48) Xie, Y.; Schaefer, H. F., III. *J. Chem. Phys.* **1993**, *98*, 8829.
- (49) Sander, R. *Compilation of Henry's Law Constants for Inorganic and Organic Species of Potential Importance in Environmental Chemistry*; <http://www.mpc-mainz.mpg.de/~sander/res/henry.html>, 1999.
- (50) Autrey, T.; Brown, A. K.; Camaioni, D. M.; Dupuis, M.; Foster, N. S.; Getty, A. *J. Am. Chem. Soc.* **2004**, *126*, 3680.
- (51) Ohshima, Y.; Sato, K.; Sumiyoshi, Y.; Endo, Y. *J. Am. Chem. Soc.* **2005**, *127*, 1108.
- (52) Meerts, W. L.; Stolte, S.; Dymanus, A. *Chem. Phys.* **1977**, *19*, 467.
- (53) Mack, K. M.; Muentner, J. S. *J. Chem. Phys.* **1977**, *66*, 5278.
- (54) Maroulis, G. *J. Chem. Phys.* **1994**, *101*, 4949.
- (55) Maroulis, G. *J. Chem. Phys.* **1999**, *111*, 6846.
- (56) Andersson, K.; Borowski, P.; Fowler, P. W.; Malmqvist, P.-A.; Roos, B. O.; Sadlej, A. J. *Chem. Phys. Lett.* **1992**, *190*, 367.
- (57) Jorgensen, W. L.; Maxwell, D. S.; Tirado-Rives, J. *J. Am. Chem. Soc.* **1996**, *118*, 11225.
- (58) Tachikawa, H.; Abe, S. *Inorg. Chem.* **2003**, *42*, 2188.
- (59) Gillies, J. Z.; Gillies, C. W.; Suenram, R. D.; Lovas, F. J.; Schmidt, T.; Cremer, D. *J. Mol. Spectrosc.* **1991**, *146*, 493.
- (60) Rowlinson, J. S.; Widom, B. *Molecular Theory of Capillarity*; Clarendon Press: Oxford, U.K., 1982.
- (61) Defay, R.; Prigogine, I. *Surface Tension and Adsorption*; Wiley: New York, 1966.
- (62) Petersen, P. B.; Saykally, R. J., Personal communication.
- (63) Li, Z. X.; Lu, J. R.; Styrkas, D. A.; Thomas, R. K.; Rennie, A. R.; Penfold, J. *Mol. Phys.* **1993**, *80*, 925.
- (64) Matsumoto, M.; Kataoka, Y. *J. Chem. Phys.* **1989**, *90*, 2398.
- (65) Tarek, M.; Tobias, D. J.; Klein, M. L. *J. Chem. Soc., Faraday Trans.* **1996**, *92*, 559.
- (66) Benjamin, I. *J. Chem. Phys.* **1999**, *110*, 8070.
- (67) Petersen, M. K.; Iyengar, S. S.; Day, T. J. F.; Voth, G. A. *J. Phys. Chem. B* **2004**, *108*, 14804.
- (68) Chandler, D. *Introduction to Modern Statistical Mechanics*; Oxford University Press: Oxford, U.K., 1987.
- (69) Vassilev, P.; Louwerse, M. J.; Baerends, E. J. *Chem. Phys. Lett.* **2004**, *398*, 212.
- (70) Khalack, J. M.; Lyubartsev, A. P. *J. Phys. Chem. A* **2005**, *109*, 378.
- (71) VandeVondele, J.; Sprik, M. *Phys. Chem. Chem. Phys.* **2005**, *7*, 1363.
- (72) Ferrario, M.; Haughney, M.; McDonald, I. R.; Klein, M. L. *J. Chem. Phys.* **1990**, *93*, 5156.
- (73) Meng, E. C.; Kollman, P. A. *J. Phys. Chem.* **1996**, *100*, 11460.
- (74) Zapalowski, M.; Bartczak, W. M. *Comput. Chem.* **2000**, *24*, 459.
- (75) Tuckerman, M. E.; Marx, D.; Parrinello, M. *Nature* **2002**, *417*, 925.
- (76) Asthagiri, D.; Pratt, L. R.; Kress, J. D.; Gomez, M. A. *Proc. Natl. Acad. Sci. U.S.A.* **2004**, *101*, 7229.
- (77) Taylor, R. S.; Dang, L. X.; Garrett, B. C. *J. Phys. Chem.* **1996**, *100*, 11720.
- (78) Dang, L. X.; Garrett, B. C. *Chem. Phys. Lett.* **2004**, *385*, 309.
- (79) Li, Y. Q.; Davidovits, P.; Shi, Q.; Jayne, J. T.; Kolb, C. E.; Worsnop, D. R. *J. Phys. Chem. A* **2001**, *105*, 10627.
- (80) Saecker, M. E.; Nathanson, G. M. *J. Chem. Phys.* **1993**, *99*, 7056.
- (81) Benjamin, I.; Wilson, M. A.; Pohorille, A. *J. Chem. Phys.* **1994**, *100*, 6500.
- (82) Benjamin, I.; Wilson, M. A.; Pohorille, A.; Nathanson, G. M. *Chem. Phys. Lett.* **1995**, *243*, 222.

- (83) Hanson, D. R.; Burkholder, J. B.; Howard, C. J.; Ravishankara, A. R. *J. Phys. Chem.* **1992**, *96*, 4979.
- (84) Takami, A.; Kato, S.; Shimono, A.; Koda, S. *Chem. Phys.* **1998**, *231*, 215.
- (85) Muller, B.; Heal, M. R. *Phys. Chem. Chem. Phys.* **2002**, *4*, 3365.
- (86) Benjamin, I. *Chem. Rev.* **1996**, *96*, 1449.
- (87) Merikanto, J.; Vehkamäki, H.; Zapadinsky, E. *J. Chem. Phys.* **2004**, *121*, 914.
- (88) Tabazadeh, A.; Yokelson, R. J.; Singh, H. B.; Hobbs, P. V.; Crawford, J. H.; Iraci, L. T. *Geophys. Res. Lett.* **2004**, *31*, doi: 10.1029/2003GL018775.
- (89) Mmereki, B. T.; Donaldson, D. J. *J. Phys. Chem. A* **2003**, *107*, 11038.
- (90) Mmereki, B. T.; Donaldson, D. J.; Gilman, J. B.; Eliason, T. L.; Vaida, V. *Atmos. Environ.* **2004**, *38*, 6091.